Inorganic Chemistry

Article

pubs.acs.org/IC

Water-Catalyzed Activation of H_2O_2 by Methyltrioxorhenium: A Combined Computational–Experimental Study

Taeho Hwang,[†,#] Bryan R. Goldsmith,[†,#] Baron Peters,*[,†,‡] and Susannah L. Scott*[,†,‡]

[†]Department of Chemical Engineering and [‡]Department of Chemistry & Biochemistry, University of California, Santa Barbara, California 93106-5080, United States

Supporting Information

ABSTRACT: The formation of peroxorhenium complexes by activation of H_2O_2 is key in selective oxidation reactions catalyzed by CH_3ReO_3 (methyltrioxorhenium, MTO). Previous reports on the thermodynamics and kinetics of these reactions are inconsistent with each other and sometimes internally inconsistent. New experiments and calculations using density functional theory with the ωB97X-D and augmented def2-TZVP basis sets were conducted to better understand these reactions and to provide a strong experimental foundation for benchmarking computational studies involving MTO and its derivatives. Including solvation contributions to the free energies as well as tunneling corrections, we compute negative reaction enthalpies for each reaction and correctly predict the hydration state of all complexes in aqueous CH_3CN. New rate constants for each of the forward and reverse reactions were both measured and computed as a function of temperature, providing a complete set of consistent activation parameters. New, independent measurements of equilibrium constants do not indicate strong cooperativity in peroxide ligand binding, as was previously reported. The free energy barriers for formation of both $CH_3ReO_2(\eta^2\text{-}O_2)$ (**A**) and $CH_3ReO(\eta^2\text{-}O_2)_2(H_2O)$ (**B**) are predominantly entropic, and the former is much smaller than a previously reported value. Computed rate constants for a direct ligand-exchange mechanism, and for a mechanism in which a water molecule facilitates ligand-exchange via proton transfer in the transition state, differ by at least 7 orders of magnitude. The latter, water-assisted mechanism is predicted to be much faster and is consequently in much closer agreement with the experimentally measured kinetics. Experiments confirm the predicted catalytic role of water: the kinetics of both steps are strongly dependent on the water concentration, and water appears directly in the rate law.

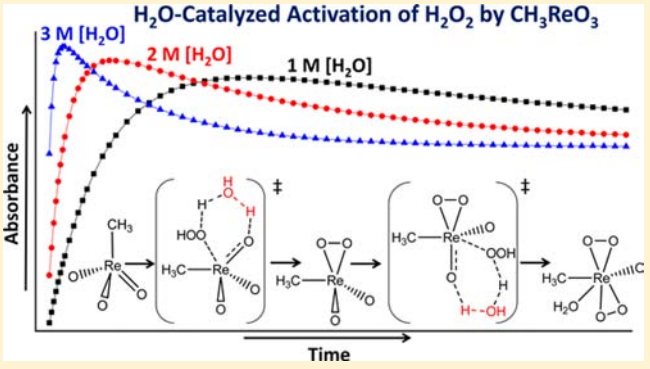

INTRODUCTION

CH_3ReO_3 (methyltrioxorhenium, MTO) has been the subject of sustained research interest for more than two decades, due to its unusual electronic structure,[1−9] its remarkable kinetic stability even in aqueous, acidic environments,[4,10−13] and its ability to catalyze a wide variety of valuable processes, ranging from olefin metathesis,[14−17] to aldehyde olefination,[18−21] oxygen atom transfer,[4,11,22−25] biomass deoxydehydration,[26−29] and even alkane functionalization.[30,31]

The best-studied reactions to-date involve the sequential, reversible complexation of MTO by 2 equiv of H_2O_2, eqs 1 and 2, leading to an equilibrated mixture of the discrete η^2-peroxo complexes **A** and **B**.[4,10,12,13,32,33]

$$\mathrm{MTO} + \mathrm{H_2O_2} \underset{k_{-1}}{\overset{k_1}{\rightleftharpoons}} \underset{\mathbf{A}}{\mathrm{CH_3ReO_2}(\eta^2\text{-}\mathrm{O_2})} + \mathrm{H_2O} \quad (1)$$

$$\mathbf{A} + \mathrm{H_2O_2} \underset{k_{-2}}{\overset{k_2}{\rightleftharpoons}} \underset{\mathbf{B}}{\mathrm{CH_3ReO}(\eta^2\text{-}\mathrm{O_2})_2(\mathrm{H_2O})} \quad (2)$$

Both **A** and **B** are kinetically competent in the selective oxidation of a very broad range of substrates, including alkenes, alkynes, alcohols, aldehydes, ketones, amines, imines, sulfides, phosphines, arsines, stibines, halides, alkanes, and arenes.[34] Moreover, many of these reactions take place under nominally "green" reaction conditions: in water or other unconventional (e.g., ionic liquid)[35] solvents, at mild temperatures, generating H_2O as the innocuous byproduct of H_2O_2 oxidation[36] (although current commercial production of H_2O_2 is far from green,[37] and cleanup of the spent H_2O solvent prior to disposal can be problematic).[38] Unlike many other oxidation catalysts, CH_3ReO_3 does not promote the competing disproportionation of H_2O_2.[17] Nevertheless, large-scale applications have proven elusive, since very high productivities are generally required to justify the use of Re, a rare and expensive metal.[39]

The structures and reactivities of **A** and **B** have been described in a number of experimental papers. Kinetic parameters for their formation from MTO have been evaluated in several different solvent systems,[10,12,13,32,33,35,40−42] with the most complete data available for aqueous acetonitrile.[32] The

Received: May 28, 2013
Published: November 21, 2013

 © 2013 American Chemical Society

peroxo complexes are readily observed by UV−vis and ^{1}H NMR spectroscopies, both of which have been used to investigate rates and measure equilibrium constants for this system. A striking cooperativity in peroxide binding is often reported, manifested in reported equilibrium constants for eq 2 that greatly exceed those for eq 1.[10,25,32,42] This effect was attributed to changes in coordination geometry and bonding at Re.

The ligand exchange reactions have also been studied computationally.[2,9,43−45] The small size of MTO and its well-behaved reactivity make it especially suited to computational investigation. Gisdakis et al. computed optimized structures for **A**, **B**, and their water adducts, as well as various transition state structures for ethylene epoxidation by the peroxo complexes.[2] Karlsson and Privalov calculated optimized structures for **B** and **B′** (the latter without a coordinated H_2O ligand) and predicted an oxygen-rebound mechanism for the oxidation of ethers, alcohols, and unfunctionalized hydrocarbons.[45] Gonzales et al. computed enthalpies for the conversion of MTO to **A**, of **A** to **B**.[9]

Two groups[9,43] calculated energy barriers and transition state geometries for the direct ligand exchange mechanism initially proposed by Pestovsky et al.[41] (in the references below, the level of theory used in each prior computational study is described). In both reports, the predicted activation enthalpies for both ligand exchange reactions exceed 100 kJ mol^{-1}, far in excess of the experimental activation enthalpies (24.5 and 29.0 kJ mol^{-1}) reported in aqueous CH_3CN.[32] Some of the discrepancy may have arisen because the role of water was not considered explicitly. In experiments, water is usually present, either as part of the solvent, or introduced with the H_2O_2 reagent. However the water concentration is often uncontrolled or neglected completely. No experimental studies to date have determined the water concentration dependence of the rate laws or equilibria. Yet the liberation of a water molecule in eq 1 makes its concentration a key kinetic and thermodynamic parameter in these reversible reactions.[13,32,46]

Water is known to catalyze proton transfer reactions in organic,[47,48] organocatalytic,[49] and biosynthetic pathways.[50−53] Water molecules participate in and accelerate many atmospheric reactions, both homogeneous (in the gas phase) and heterogeneous.[54−58] Trace water may increase rates of proton migration in zeolites by up to 10^{26} times[59] and is implicated in key catalytic steps of the methanol-to-gasoline process.[60,61] Recently, activation energies for glucose isomerization and fragmentation by retro-Aldol condensation were calculated to be considerably lower for water-mediated bimolecular pathways, compared to the unimolecular processes.[62] Water was shown to promote the reaction of electrochemically generated $C_5H_6N\bullet$ with CO_2.[63] There is also a growing body of evidence for water participation in transition states involving metal complexes, where it acts as a cocatalyst for reactions such as the transfer hydrogenation of ketones,[64] CO_2 hydrogenation,[65] and water oxidation.[66] In a recent computational study, and following a suggestion by Wang and Espenson,[32] Kuznetsov and Pombeiro suggested that water may play an important role in the mechanism of ligand exchange at MTO.[43]

Accurate kinetic and thermodynamic data are required to benchmark computational models. The models can then be used to predict more complex mechanisms involving MTO, such as olefin metathesis. Unfortunately, the published experimental results for the reactions of MTO with H_2O_2 are neither complete nor consistent. For example, the only activation parameters reported for this reaction yield a rate constant k_1 for the formation of **A** that is 2 orders of magnitude lower than the value reported at 25.0 °C in the same paper.[32] Furthermore, the rate constants k_{-1} and k_{-2} have never been directly measured in any solvent system; their calculation from rate constants for the forward reactions and equilibrium constants precludes important consistency checks.[32] Reaction and activation enthalpies and entropies for the reverse reactions have never been measured.

Therefore we undertook to evaluate all of the kinetic and thermodynamic parameters for the MTO/H_2O_2 reaction system. Although reactions involving proton transfer in water are very challenging for density functional theory (DFT), our results clearly confirm the key role of water. This has implications for the rates and mechanisms of catalytic processes, including MTO-catalyzed selective oxidations, in which ligand protonolysis is a key step.

COMPUTATIONAL METHODS

All electronic structure calculations were performed using Gaussian 09.[67] An appropriate DFT model for Re requires a relativistic effective core potential,[68−70] a valence shell with d- and f-orbitals,[71] a density functional capable of accurately describing electron correlation, and for the reactions studied here, the ability to model solvent effects. The range-separated ωB97X-D density functional was chosen.[72] We acknowledge that ωB97X-D is, like many other modern functionals,[73,74] not truly ab initio through its use of 18 optimized training set parameters. Furthermore, it uses an empirical dispersion correction (-D), a physically motivated correction added after the SCF calculation. Nevertheless, among DFT functionals, multiple benchmark studies have found ωB97X-D to be among the five best.[75,76] It has been reported to give low, unsigned mean errors for computed ground-state energetics,[72,74−78] activation barriers,[76,77] and nonbonded interactions.[72] However, since MTO and its derivatives are very different from the training sets used to parametrize ωB97X-D, actual errors may be larger than the mean absolute deviations reported in the studies cited above.

Standard def2-TZVP basis sets for each element were obtained from the EMSL basis set exchange.[79,80] We reoptimized the standard atomic f-orbital and augmented this with a second f-orbital. The two f-orbital coefficients were optimized to minimize the electronic energy of the perrhenate anion, ReO_4^-. The optimal f-exponents were found to be 0.4 and 1.0, nearly equal to those obtained by Pietsch et al.[3] for an uncontracted LANL2DZ Re basis.[70,81] The basis set resulting from geometry optimization of the perrhenate ion will henceforth be denoted aug-def2; the corresponding Gaussian input is given in Table S1 of the Supporting Information. The aug-def2 basis set is similar to that of Pietsch et al.,[3] but it uses a Stuttgart effective core potential[69] instead of the Hay-Wadt effective core potential.[70] Note that other large bases for Re have been developed,[68,82,83] some of which even include h-functions and beyond,[83] which may further improve computational accuracy.

Reported free energies include rotational, translational, vibrational, and zero-point contributions, Table S2, Supporting Information.[84] Following Wertz,[85] the entropic contribution to the free energy was corrected for solvation in acetonitrile, using the procedure of Kuznetsov and Pombeiro.[43] The reference state for all species is 1 M. A single-point conductor-type polarizable continuous medium (CPCM) solvent correc-

dx.doi.org/10.1021/ic401343m | Inorg. Chem. 2013, 52, 13904−13917

tion[86,87] was used to model the polarizing dielectric of the mixed water-acetonitrile solvent. Gaussian 09 default parameters were used, except that the solvent dielectric was set to that of acetonitrile. In a recent benchmarking study,[88] the CPCM model approximated solvation free energies to within 11 kJ mol^{-1} of the experimental values. While H_2O is part of the implicit solvent, H_2O was also treated as an explicit reactant in DFT calculations for those reactions in which water is an active participant. Transition states were optimized using the eigenvector-following algorithm.[89−91] Each transition state structure has a single imaginary frequency. Energies, CPCM-corrected energies, and zero-point energies are given for all species in Table S3, Supporting Information. Cartesian coordinates are listed in Table S4, Supporting Information.

Because all of the reactions investigated here involve proton transfer, rate constants were computed using transition state theory[92] with a tunneling correction, $k = \Gamma(T)k_BT/h \exp[-\Delta G^{\ddagger}/k_BT]$. Although more accurate tunneling corrections exist for transition states,[93−97] the truncated parabolic tunneling correction[96] was used since most tunneling corrections were of order one (Table S5, Supporting Information). Solvation-induced changes to the imaginary frequencies were not considered in the tunneling corrections. Imaginary frequencies and tunneling corrections are given in Table S5 of the Supporting Information. To include the effect of tunneling in our comparisons with experiment, the computed values of $\Delta H^{\ddagger}$ and $\Delta S^{\ddagger}$ were not obtained directly from partition functions. Instead, we computed rate constants at different temperatures (with tunneling corrections) and extracted activation parameters from Eyring plots, similar to the method used to obtain experimental values of $\Delta H^{\ddagger}$ and $\Delta S^{\ddagger}$. For comparison, activation parameters obtained according to the usual harmonic transition state theory formulas,[98] which do not incorporate tunneling, are provided in Table S6 of the Supporting Information. Since the experimental activation parameters necessarily include tunneling, the apparent $\Delta H^{\ddagger}$ and $\Delta S^{\ddagger}$ values obtained from our computed Eyring plots (in Tables 4 and 5) are required for direct comparison to the experimental values. Table S6, Supporting Information, shows that the effects of including tunneling are substantial. The thermodynamic parameters ΔH and ΔS were extracted analogously, from van't Hoff plots. Table S10, Supporting Information, shows that the resulting values are essentially identical to those obtained directly from partition functions at room temperature.

Solvation free energies were computed only at 298 K. Temperature-dependent continuum solvation corrections can be obtained via more complicated Langevin Dipoles,[99,100] SM8T,[101] or COSMO-RS[102,103] calculations. However, our experiments involve a narrow range of reaction temperatures, for which the absolute solvation free energies are expected to change only slightly with temperature. Moreover, we expect a cancellation of changes in the absolute solvation free energies to further minimize temperature-dependent solvation effects. For example, if MTO and H_2O_2 are more strongly solvated at low temperatures, then **A** and H_2O are probably also more strongly solvated at low temperatures. For these reasons, we did not include temperature-dependent solvation.

Computed rate constants were multiplied by the experimental water concentration, as appropriate, to obtain pseudo-rate constants and apparent equilibrium constants for comparison to experimental values. A detailed description of this procedure is given in the Supporting Information. All computed enthalpies and free energies are reported to the nearest integer kJ mol^{-1}, and entropies to the nearest integer J mol^{-1} K^{-1}, to avoid overstating the computational accuracy. However, to ensure that others can precisely reproduce our calculations, tables containing more significant figures are provided in the Supporting Information.

EXPERIMENTAL METHODS

Materials. CH_3ReO_3 (MTO, Aldrich), H_2O_2 (31.9 wt % aqueous solution, EMS Chemicals), CH_3CN (HPLC grade, Fisher), CD_3CN (99.8%, Cambridge Isotope Laboratories, Inc.), and $HClO_4$ (70 wt %, Aldrich) were used as received. The H_2O_2 and $HClO_4$ stock solutions were diluted with deionized water; the former was standardized by iodometric titration.

UV−Visible Spectroscopic Methods. Time-resolved kinetic data for the formation of the peroxo complexes **A** and **B** in aqueous CH_3CN were acquired under pseudo-first-order reaction conditions ($[H_2O_2]_0 > [MTO]_0$) at constant temperature (±0.1 °C) using a Shimadzu UV-2401PC spectrophotometer.[32] The initial MTO concentration was 1.0 mM, while the concentration of H_2O_2 was varied systematically in the range 8.4−41.3 mM. Upon mixing colorless solutions of MTO and H_2O_2, a yellow color appears that is largely due to the formation of **B**, with a maximum absorbance at 360 nm.[10] The maximum in absorbance for the intermediate **A** occurs at 320 nm.[32] Absorbance-time profiles were recorded simultaneously at both wavelengths in square quartz cuvettes (Precision Cells, Inc., 10 mm optical path length). Water was inevitably introduced in variable amounts along with the aqueous H_2O_2 reagent. Since its concentration affects the reaction kinetics, $[H_2O]$ was always adjusted to the desired value (usually, 2.0 M to match a previous UV−vis study)[32] by adding a precise amount of water.

Rate constants were extracted from the biphasic kinetic profiles by nonlinear least-squares curve-fitting, using either eq 3 (at 320 nm) or eq 4 (at 360 nm):

$$\mathrm{Abs}_t = \mathrm{Abs}_\infty + \alpha(1 - e^{-k_{fast}t}) + \beta e^{-k_{slow}t} \quad (3)$$

$$\mathrm{Abs}_t = \mathrm{Abs}_\infty + \alpha e^{-k_{fast}t} + \beta e^{-k_{slow}t} \quad (4)$$

where Abs_t is the absorbance at time t, Abs_∞ is the final absorbance, and k_{fast} and k_{slow} are the pseudo-first-order rate constants which describe the biexponential time course of the sequential ligand exchange reactions. The physical meanings of the coefficients α and β are given by eq 5 and 6:[104]

$$\alpha = \frac{(\varepsilon_A - \varepsilon_{MTO})k_{fast} - (\varepsilon_{MTO} - \varepsilon_B)k_{slow}}{k_{slow} - k_{fast}}[MTO]_0 \quad (5)$$

$$\beta = \frac{(\varepsilon_B - \varepsilon_A)k_{fast}}{k_{slow} - k_{fast}}[MTO]_0 \quad (6)$$

where ε_A, ε_B, and ε_{MTO} are the molar extinction coefficients of **A**, **B**, and MTO, respectively, at the specified measurement wavelength, and $[MTO]_0$ is the initial concentration of MTO. In the kinetic analyses, α and β were treated as curve-fit parameters. For all data transformations, including the van't Hoff and Eyring plots used to obtain thermodynamic and kinetics parameters, the stated uncertainties are based on full statistical error propagation.

Equilibrium constants were extracted from kinetic measurements, and (independently) from eq 7, which describes the dependence of the final absorbance at 360 nm on the equilibrium concentration of H_2O_2.[35,42]

$$\frac{\mathrm{Abs}_{360,final}}{[Re]_{total}} = \frac{\varepsilon_{A,360}K_1'[H_2O_2] + \varepsilon_{B,360}K_1'K_2[H_2O_2]^2}{1 + K_1'[H_2O_2] + K_1'K_2[H_2O_2]^2} \quad (7)$$

At this wavelength, neither H_2O_2 nor MTO contributes significantly to the absorbance.[10] The version of eq 7 that appears in the literature includes an equilibrium constant called K_1 that does not acknowledge

the release of a H_2O molecule in eq 1. Here, we label this variable K_1' instead (where $K_1' = K_1/[H_2O]$).

^{1}H NMR Spectroscopic Methods. The reaction between MTO and H_2O_2 was also investigated by recording ^{1}H NMR spectra on an Avance DMX500 NMR spectrometer at precise time intervals. In kinetics experiments, the initial MTO and H_2O_2 concentrations were 13.0 mM and 140 mM, respectively, in CD_3CN, while the concentration of H_2O was varied in the range 0.04−2.5 M. CH_3OH formation was suppressed in the presence of excess $[H_2O_2]_0$[32] and by adding 0.100 M $HClO_4$. The kinetics of peroxo complex formation are reported to be pH-independent.[10] Precise values for the chemical shifts have not been published, but the usual order $\delta(\mathbf{B}) > \delta(\mathbf{A}) > \delta$ (MTO) observed in other solvents[33] was reported to be different in aqueous CD_3CN.[32] In the presence of 2.6 M H_2O (reproducing the solvent mixture used in a previous NMR study),[32] we observed $\delta(\mathbf{B}) = 2.812$ ppm, δ(MTO) = 2.603 ppm, and $\delta(\mathbf{A}) = 2.559$ ppm.

The order of the chemical shifts is $[H_2O]$-dependent. All three signals shift upfield, but to different extents, as the water concentration increases. Assignments were therefore based on kinetic profiles. The intensity of the signal for **B**, in the region 2.80−2.90 ppm, increases steadily over the entire reaction period. The signals for MTO and **A** both appear in the region 2.55−2.75 ppm, with $\delta(\mathbf{A}) > \delta$(MTO) for $[H_2O] < 1.0$ M. However, the signal for **A** is more sensitive to $[H_2O]$ than that of MTO, causing their relative positions to change as $[H_2O]$ increases. The MTO signal decreases in intensity monotonically, while the intensity of the signal for **A** increases then decreases during the reaction.

Nonlinear least-squares curve-fitting to the kinetic profiles based on the ^{1}H NMR signals was used to obtain the observed rate constants k_{fast} and k_{slow}. Decomposition of **A** to CH_3OH (δ 3.30 ppm) can compete with the conversion of **A** to **B** at the higher MTO concentrations required by the ^{1}H NMR experiments.[13,22,32] However, the resulting observed rate constants were similar (albeit less precise) to those measured by UV−vis spectroscopy. CH_3OOH (δ 3.78 ppm) was observed to form (due to decomposition of **B**)[10,32] only on much longer time scales (several days).

We also attempted to extract equilibrium constants from the ^{1}H NMR data.[32] However, upon reproducing reaction conditions reported in the literature (13.0 mM MTO, 140.0 mM H_2O_2, and 2.6 M H_2O in CD_3CN, 27.0 °C), the equilibrium concentrations of MTO and **A** were difficult to measure due to their very low signal intensities. With less water (ca. 2.0 M, to match the UV−vis experiments), the weak, overlapping signals for MTO and **A** could not be integrated accurately. Consequently, equilibrium constants based on the NMR method were deemed highly uncertain.

RESULTS AND DISCUSSION

Computational Modeling of the Sequential Reactions between MTO and H_2O_2. We first computed structures for MTO and the products of its ligand exchange reactions with 2 equiv of H_2O_2, corresponding to eqs 1 and 2. In addition to the observable η^2-peroxo complexes **A** and **B**, there are two intermediate, nonobservable η^1-hydroperoxo complexes, shown in Figure 1. $\mathbf{I_1}$ is formed by coordination of H_2O_2 to MTO, accompanied by transfer of a single proton to an adjacent oxo ligand. $\mathbf{I_2}$ is formed in an analogous manner, via reaction of H_2O_2 with **A**. The same intermediates were first proposed by Espenson and co-workers;[4] their structures were first computed by Gonzales et al.[9] Figure 1 shows free energies computed for all stable species, relative to *noninteracting* MTO, H_2O and H_2O_2. They include CPCM and entropic corrections for solvation in CH_3CN.[43,85] Since we compute both MTO·H_2O and MTO·H_2O_2 to be less stable than MTO (by 18 and 16 kJ mol^{-1}, respectively, in the presence of 1 M H_2O), non-interacting reactants are the appropriate choice of starting point for computing thermodynamic and kinetic parameters.

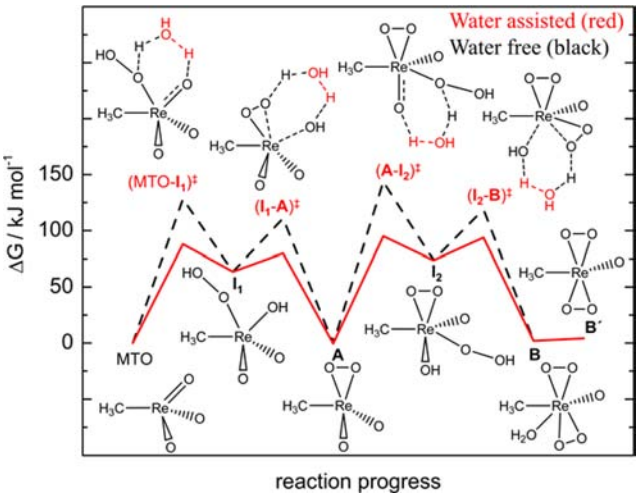

Figure 1. Free energies, including CPCM and entropic corrections for solvation in CH_3CN,[43,85] at 25.0 °C (with all species at 1.0 M concentration) for formation of the peroxo complexes of MTO. Each transition state (shown here as the water-assisted version) is identified by a hyphen between the reactant and product states of the Re complex. Unbound H_2O_2 and H_2O are omitted for clarity. Dashed black and solid red lines show free energies without and with water-assisted transition states, respectively.

The same is true for the intermediate **A**, which our calculations predict to be more stable than **A**·H_2O by 11 kJ mol^{-1} at 25 °C in the presence of 1 M H_2O. An experimental study reported no NMR signals for water coordinated to **A** in the temperature range −55 to 20 °C.[13] In contrast, Gisdakis et al. calculated a very favorable enthalpy for water binding,[2] while Kuznetsov and Pombeiro computed the free energy of **A**·H_2O to be lower than for **A** (by 9 kJ mol^{-1} in aqueous CH_3CN with 1 M H_2O).[43] Gonzales et al. reported a small binding enthalpy for H_2O[9] but argued that **A** should be more stable than **A**·H_2O based on entropic considerations.

Signals assigned to a labile water molecule coordinated to **B** have been observed by both ^{1}H and ^{17}O solution-state NMR.[13,105] Although not necessarily relevant to the solution-state structure, a solid was isolated with the expected composition of **B** (CH_5O_6Re), and a crystal structure was obtained that includes this bound water molecule as well as a hydrogen-bonded diglyme molecule.[40] In agreement with these experimental findings and with previous calculations,[2,9,43] we predict the free energy of **B** to be slightly lower (by 3 kJ mol^{-1}) than that of **B′** at 25 °C in the presence of 1 M H_2O.

Table 1 compares our computed thermodynamic parameters for the ligand exchange reactions with those calculated by others, as well as with previously published experimental values.[32] For the formation of **A** from MTO, our computed reaction enthalpy and free energy are both slightly negative in 1 M H_2O at 25 °C, as are the reported experimental values.[32] In contrast, Kuznetsov and Pombeiro calculated a positive reaction enthalpy for the formation of **A** in aqueous acetonitrile, and computed ΔG_1 to be uphill by 10 kJ mol^{-1} at 25 °C.[43] Gisdakis et al. reported that the enthalpy of reaction in the gas phase is positive unless water remains bound, as **A**·H_2O.[2] Gonzales et al. calculated a positive reaction enthalpy in THF.[9] The improved thermodynamic description given by our computational model lends confidence to our predictions about reaction intermediates, the extent to which they accumulate during the reaction, and the kinetics of their interconversion.

dx.doi.org/10.1021/ic401343m | Inorg. Chem. 2013, 52, 13904−13917

Table 1. Comparison of Computed and Experimental Thermodynamic Parameters[a] for the Reversible Formation of A and B, via the Reactions of MTO with H_2O_2

	calculated[b]				experimental[f]	
param	ref 2[c]	ref 9	ref 45[c,d]	this work	ref 32[h]	this work[g]
ΔH_1	5	15	5	−4		−12.31 (177)
ΔS_1	*e*	*e*	−15	−12	*h*	6.80 (9)
ΔG_1	*e*	*e*	10	−1	−13.2	−14.34 (207)
ΔH_2	−41	−1	−36	−24	*h*	−32.82 (523)
ΔS_2	*e*	*e*	−121	−88	*h*	−70.60 (309)
ΔG_2	*e*	*e*	0	2	−16.1	−11.77(195)

[a]Enthalpies and free energies are reported in kJ mol^{-1}, entropies in J K^{-1} mol^{-1}. Free energies were computed or measured at 25 °C. Extra significant figures are provided for experimental values to facilitate interconversion of thermodynamic parameters, as recommended in ref 104. [b]The values pertain to species in the gas phase,[2] in aqueous THF,[9] or in aqueous CH_3CN containing 1 M H_2O (ref 45 and our work). [c]Based on values reported for **A**, even though **A**·H_2O was predicted to be more stable. [d]Considering **A**·H_2O as the product/reactant instead, the reported thermodynamic parameters are ΔH_1 = −32 kJ mol^{-1}, ΔS_1 = −111 J K^{-1} mol^{-1}, ΔH_2 = 1 kJ mol^{-1} and ΔS_2 = −24 J K^{-1} mol^{-1}.[45] [e]Computed reaction entropies and free energies were not reported. [f]Measured in aqueous CH_3CN containing 2.6 M H_2O (ref 32) or 2.0 M H_2O (this work). [g]Values and their uncertainties (shown in parentheses) were obtained from the van't Hoff analyses shown in Figure 7. [h]Experimental reaction entropies and enthalpies were not reported.

For the transformation of **A** to **B**, our computational model predicts ΔH_2 = −24 kJ mol^{-1} and ΔS_2 = −88 J K^{-1} mol^{-1}. For comparison, Gonzales et al. computed a negligible reaction enthalpy for this step (−1 kJ mol^{-1}) in THF.[9] Acknowledging that, in reality, the reaction must be significantly exothermic (since the enthalpy change must overcome the loss of translational entropy involved in coordinating H_2O_2 without displacing another ligand), they proposed strong H-bonding to two THF molecules to provide the required additional enthalpic stabilization for **B**. Specifically, they report that such H-bonding yields an enthalpy change of −18 kJ mol^{-1}, in excellent agreement with the experimental ΔG of −17.6 kJ mol^{-1}. However, this explanation ignores the substantial loss of entropy involved in creating a bound complex from three unassociated molecules in solution. In contrast, Kuznetsov and Pombeiro reported an even more negative reaction enthalpy than ours, and despite an unfavorable entropy change, predicted ΔG_2 to be 0.0 kJ mol^{-1} at 25 °C.[43]

Despite the negative value of our calculated reaction enthalpy, we still failed to predict a favorable equilibrium constant for eq 2. Our computed value of ΔG_2, 2 kJ mol^{-1} at 25 °C, exceeds the reported experimental value (−16.1 kJ mol^{-1})[32] by ca. 18 kJ mol^{-1}. However, our new experimental measurements (see below) reduce the discrepancy, such that ΔG_1 and ΔG_2 are overestimated computationally by similar amounts. As discussed below, our calculations and our experiments both find $\Delta G_1 < \Delta G_2$ at room temperature, in contrast to previous experiments which reported cooperative binding of peroxide to MTO with $\Delta G_1 > \Delta G_2$.[4,32]

Computed Ligand Exchange Kinetics. Two potential reaction mechanisms for the ligand exchange reactions were investigated: with, and without, water-assisted transition states. Their energy profiles are compared in Figure 1. We used our results to predict the kinetics of peroxo complex formation as follows. The apparent rate constants k_1 and k_2, as defined in eqs 1 and 2, can be related to the calculated rate constants for the reaction steps using the quasi-steady-state approximations shown in eqs 8 and 9:

$$k_1 = \frac{k_{\mathrm{MTO}\rightarrow \mathrm{I}_1} k_{\mathrm{I}_1\rightarrow \mathrm{A}}}{k_{\mathrm{I}_1\rightarrow \mathrm{MTO}} + k_{\mathrm{I}_1\rightarrow \mathrm{A}}} \quad (8)$$

$$k_2 = \frac{k_{\mathrm{A}\rightarrow \mathrm{I}_2} k_{\mathrm{I}_2\rightarrow \mathrm{B}}}{k_{\mathrm{I}_2\rightarrow \mathrm{A}} + k_{\mathrm{I}_2\rightarrow \mathrm{B}}} \quad (9)$$

On the basis of our free energy calculations, the reactions of the intermediates I_1 and I_2 are much faster in the forward directions than in the reverse directions at 25 °C (i.e., $k_{\mathrm{I}_1\rightarrow \mathrm{A}} \gg k_{\mathrm{I}_1\rightarrow \mathrm{MTO}}$ and $k_{\mathrm{I}_2\rightarrow \mathrm{B}} \gg k_{\mathrm{I}_2\rightarrow \mathrm{A}}$). The expressions in eq 8 and 9 therefore simplify to

$$k_1 \approx k_{\mathrm{MTO}\rightarrow \mathrm{I}_1} \quad (10)$$

$$k_2 \approx k_{\mathrm{A}\rightarrow \mathrm{I}_2} \quad (11)$$

We note that these rate constants include, implicitly, the unfavorable pre-equilibrium constants involved in coordinating H_2O_2 to MTO and **A**.[106−109] The appropriate expressions for k_{-1} and k_{-2} can be written simply by enforcing detailed balances (i.e., invoking microscopic reversibility).

Next, the rate constants for the conversion of MTO to **A**, and **A** to **B**, were computed with tunneling corrections for three different temperatures, spanning the range used in our experiments. At 25 °C, the resulting values of both k_1 (1×10^{-8} M^{-1} s^{-1}) and k_2 (4×10^{-10} M^{-1} s^{-1}) for transition states *without water assistance* are slower than the reported experimental rate constants[32] by at least 7 orders of magnitude. Computed apparent rate constants were used to construct Eyring plots, in order to extract apparent activation parameters that include tunneling effects. Activation enthalpies for the mechanism without water assistance or tunneling, $\Delta H_1^{\ddagger}$ = 104 kJ mol^{-1} and $\Delta H_2^{\ddagger}$ = 116 kJ mol^{-1}, are comparable to values calculated by others,[9,43] but much higher than the reported experimental values: $\Delta H_1^{\ddagger}$ = 24.5 kJ mol^{-1} and $\Delta H_2^{\ddagger}$ = 29.0 kJ mol^{-1}.[32] Furthermore, our computed activation entropies, $\Delta S_1^{\ddagger}$ = −81 J K^{-1} mol^{-1} and $\Delta S_2^{\ddagger}$ = −94 J K^{-1} mol^{-1}, are considerably less negative than the reported experimental values: $\Delta S_1^{\ddagger}$ = −212 J K^{-1} mol^{-1} and $\Delta S_2^{\ddagger}$ = −214 J K^{-1} mol^{-1}.[32] Including the effects of tunneling reduces the computed enthalpies by over 20 kJ mol^{-1}, to $\Delta H_1^{\ddagger}$ = 84 kJ mol^{-1} and $\Delta H_2^{\ddagger}$ = 78 kJ mol^{-1}, and makes computed entropies more negative by over 30 J K^{-1} mol^{-1}, to $\Delta S_1^{\ddagger}$ = −114 J K^{-1} mol^{-1} and $\Delta S_2^{\ddagger}$ = −161 J K^{-1} mol^{-1}. However, the computed free energy barriers are still much too large (Table S6 of the Supporting Information)

Including a single water molecule in each of the four transition states results in a significant lowering of their free energies, Figure 1. In each step, water participates directly, mediating proton transfer between the coordinated H_2O_2/HO_2^- ligand and an adjacent O^{2-}/HO^- ligand. Although the overall shapes of the Gibbs' free energy profiles are similar, all free energies of activation are lower for the water-catalyzed pathway by at least 30 kJ mol^{-1} at 25 °C. Consequently, each rate constant in the water-catalyzed pathway is predicted to be many orders of magnitude faster (specifically, seven for k_1 and k_{-1} and eight for k_2, and k_{-2}), compared to the mechanism without explicit water assistance. This dramatic acceleration of ligand exchange recalls recent computational work in which

dx.doi.org/10.1021/ic401343m | *Inorg. Chem.* 2013, 52, 13904−13917

proton relays involving noncoordinated H_2O and/or ROH dramatically lower the barriers for formation of peroxo, hydroperoxo, and alkylhydroperoxo complexes of Mo, W, and Re.[45,110] We also note the importance of tunneling in the water-assisted mechanism, which is reflected in decreases in our computed activation enthalpies and entropies of 6−10 kJ mol^{-1} and 10−22 J mol K^{-1}, respectively.

Activation parameters for the water-catalyzed pathway were obtained in a similar way. The rate expressions that correspond to the water-catalyzed mechanism, eqs 12 and 13, are shown in Table 2, which serves to define all of the rate constants.

$$\mathrm{MTO} + \mathrm{H_2O_2} + \mathrm{H_2O} \underset{k^w_{-1}}{\overset{k^w_1}{\rightleftharpoons}} \underset{\mathbf{A}}{\mathrm{CH_3ReO_2(\eta^2\text{-}O_2)}} + 2\mathrm{H_2O} \quad (12)$$

$$\mathbf{A} + \mathrm{H_2O_2} + \mathrm{H_2O} \underset{k^w_{-2}}{\overset{k^w_2}{\rightleftharpoons}} \underset{\mathbf{B}}{\mathrm{CH_3ReO(\eta^2\text{-}O_2)_2(H_2O)}} + \mathrm{H_2O} \quad (13)$$

Table 2. Rate Expressions That Define the Rate Constants in the Water-Catalyzed Mechanism[a]

directly computed	pseudo-second-order	pseudo-first-order
$k^w_1[\mathrm{MTO}][\mathrm{H_2O_2}][\mathrm{H_2O}]$	$k_1[\mathrm{MTO}][\mathrm{H_2O_2}]$	
$k^w_{-1}[\mathbf{A}][\mathrm{H_2O}]^2$	$k_{-1}[\mathbf{A}][\mathrm{H_2O}]$	$k'_{-1}[\mathbf{A}]$
$k^w_2[\mathbf{A}][\mathrm{H_2O_2}][\mathrm{H_2O}]$	$k_2[\mathrm{MTO}][\mathrm{H_2O_2}]$	
$k^w_{-2}[\mathbf{B}][\mathrm{H_2O}]$		$k_{-2}[\mathbf{B}]$

[a]The pseudo-second-order rate constants for the forward reactions and the pseudo-first-order rate constants for the reverse reactions are so-defined in order to directly compare computed and experimentally measured values.

Each of the directly computed rate constants, k^w_1, k^w_{-1}, k^w_2, and k^w_{-2}, must be multiplied by $[\mathrm{H_2O}]^n$ (n = 1, 2) for comparison to the experimentally measured pseudo-first-order and pseudo-second-order rate constants. The corresponding Eyring plots are shown in Figure 2. The calculated value of $\Delta H_1^{\ddagger}$ is reduced from 84 to 31 kJ mol^{-1} when a water molecule assists the proton transfer in (MTO-I$_1$)‡, while the apparent value of $\Delta S_1^{\ddagger}$ becomes less negative by 60 J K^{-1} mol^{-1}.

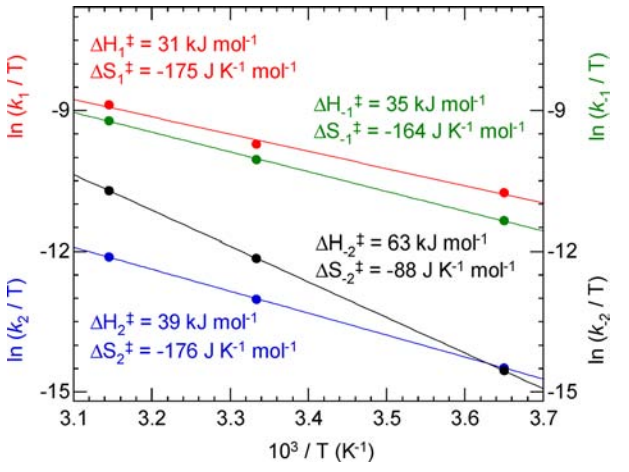

Figure 2. Eyring plots based on computed pseudo-second-order rate constant (k_1, k_{-1}, k_2) and a pseudo-first-order rate constant (k_{-2}) for the water-catalyzed mechanism, in the presence of 2.0 M H_2O (the same as the concentration used in our experiments).

Kuznetsov and Pombeiro reported a similar activation enthalpy for the water-catalyzed formation of **A** from MTO·H_2O_2 + H_2O, 28 kJ mol^{-1}, and remarked on its perfect agreement with the experimental barrier measured in water (29 kJ mol^{-1}).[45] However, this agreement is fortuitous. The mechanism includes an endoergonic pre-equilibrium step (i.e., H_2O_2 coordination) whose significant contribution they neglected to include in the effective barriers for both ligand exchange reactions. Nor did their calculations include the effect of tunneling on the activation parameters for the rate-determining proton transfer steps. Unfavorable association pre-equilibria (involving both H_2O_2 and H_2O) must be included in the effective barriers and in the calculation of apparent rate constants. Since free energy is a state function, the order of association with the Re complex is irrelevant.

Before comparing our computed kinetic parameters with experiment, we attempted to resolve apparent inconsistencies in previously published measurements.[32,33] We deemed it important to carefully control the water concentration, given its expected roles in the equilibrium and rate expressions for the water-catalyzed mechanism. In the following sections, we report new, more precise and consistent experimental measurements from which all thermodynamic and activation parameters were obtained for the reversible formation of **A** and **B**, thereby enabling direct comparison with our computed values.

Experimental Kinetics of Sequential Formation of A and B. Representative biphasic kinetic profiles, recorded by UV−vis spectroscopy for the sequential formation of **A** and **B** from MTO at 25.0 °C in CH_3CN containing 2.0 M H_2O, are shown in Figure 3 at two wavelengths, corresponding to the

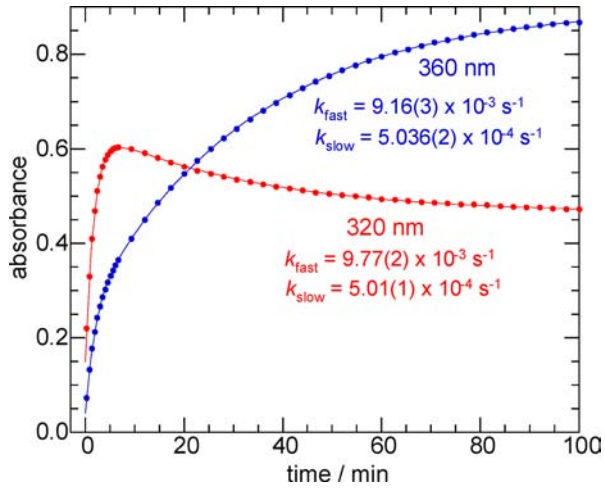

Figure 3. Time-resolved kinetic profiles, at two wavelengths, for the reaction of MTO (1.0 mM) with excess H_2O_2 (14.7 mM), recorded at 25.0 °C in CH_3CN containing 2.0 M H_2O. Ca. 6% of the measured data points in this time-interval are shown. Curve-fits were generated using all of the data, and either eq 3 (red) or eq 4 (blue).

absorbance maxima of **A** and **B**. The general appearance of these profiles is very similar to published reports. However, our data treatment differs in several significant ways. Consequently, we will describe our analysis of the experimental kinetics in some detail.

Values of the maximum intensity at 320 nm, as well as k_{fast}, increase with $[\mathrm{H_2O_2}]_0$, Figure 4. The curve-fits to the appropriate biexponential rate law (eq 3 and 4) describe the kinetic profiles well, and there is good agreement between the

dx.doi.org/10.1021/ic401343m | Inorg. Chem. 2013, 52, 13904−13917

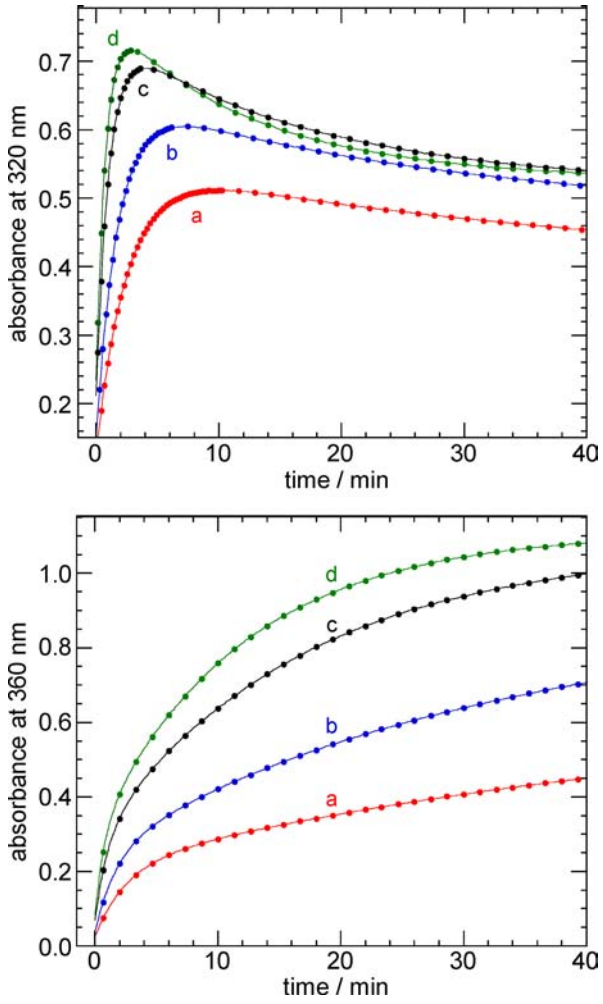

Figure 4. Time-resolved kinetic profiles, at two wavelengths, for the reactions of 1.0 mM MTO when $[H_2O_2]_0$ is (a) 8.4 mM; (b) 14.7 mM; (c) 29.6 mM; and (d) 41.3 mM. All data were recorded at 25.0 °C in CH_3CN containing 2.0 M H_2O. Only 10−20% of the measured data points collected in this time interval are shown. Curve-fits were generated using all of the data, and either eq 3 (320 nm) or eq 4 (360 nm).

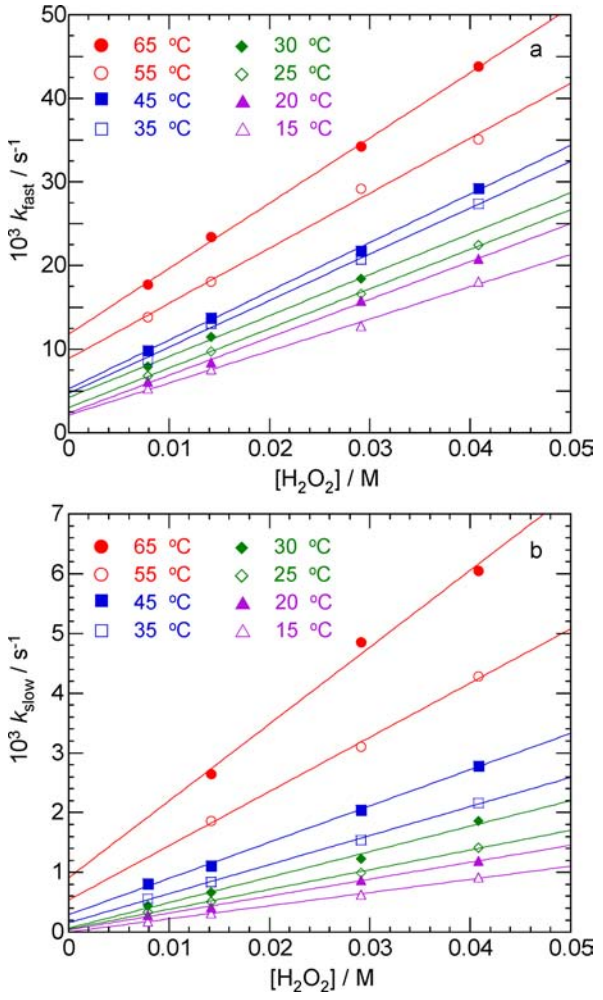

Figure 5. Dependence of the directly measured rate constants on excess $[H_2O_2]$, for (a) k_{fast}; and (b) k_{slow}, at eight different temperatures, showing linear curve-fits.

measured pseudo-first-order rate constants k_{fast} and k_{slow} so-obtained at both wavelengths. Judging by the standard errors in the fits, k_{fast} is determined somewhat more precisely at 320 nm, while k_{slow} is measured more precisely at 360 nm.

Experiments analogous to those shown in Figure 4 were performed at variable temperatures, from 15.0 to 65.0 °C. At reaction temperatures higher than 35.0 °C, the absorbance at long reaction times does not stabilize but instead declines gradually, suggesting a slow, irreversible decomposition of one or both peroxo complexes to $HReO_4$ and CH_3OH or CH_3OOH.[13,32] Truncation of the absorbance-time data sets eliminated most of this declining absorbance and gave reliable curve-fit parameters. Values for all observed rate constants are shown in Table S7 of the Supporting Information.

The plots of k_{fast} or k_{slow} vs $[H_2O_2]$ are linear with significant *y*-intercepts, Figure 5, and thus contributions from the rates of the reverse reactions (i.e., reversion of **A** to MTO, and of **B** to **A**) are not negligible, as assumed in an earlier kinetic treatment.[32] Consequently, k_{fast} and k_{slow} cannot be directly associated with k_1 and k_2. The relationships between the mechanism-based apparent rate constants for sequential reversible reactions, as defined in eqs 1 and 2, and the directly measured pseudo-first-order rate constants, are described by eqs 14 and 15.[25]

$$k_{fast} + k_{slow} = (k_1 + k_2)[H_2O_2]_0 + (k'_{-1} + k_{-2}) \quad (14)$$

$$k_{fast} \times k_{slow} = (k_1 \times k_2)[H_2O_2]_0^2 + (k_1 \times k_{-2})[H_2O_2]_0 + (k'_{-1} \times k_{-2}) \quad (15)$$

According to eq 1, the pseudo-first-order rate constant k'_{-1} must be water-dependent (i.e., $k'_{-1} = k_{-1}\,[H_2O]^n$, where $n \geq 1$).

The sums and products of k_{fast} and k_{slow} are plotted vs $[H_2O_2]$ in Figure 6, which also shows the corresponding curve-fits based on eqs 14 and 15. At each temperature, five curve-fit parameters $(k_1 + k_2)$, $(k'_{-1} + k_{-2})$, $(k_1 \times k_2)$, $(k_1 \times k_{-2})$ and $(k'_{-1} \times k_{-2})$ were extracted. The values of $(k_1 + k_2)$ and $(k_1 \times k_2)$ obtained in this way gave individual values for the pseudo-second-order rate constants k_1 and k_2, which were then used to obtain k'_{-1} and k_{-2} from the remaining fitted values.

The values of the four $[H_2O_2]$-independent rate constants at 25 °C are shown in Table 3; values for all temperatures from 15−65 °C can be found in Table S8, Supporting Information. Our k_1 value, $(0.47 \pm 0.06)\ M^{-1}\ s^{-1}$, is similar to an earlier one, $(0.81 \pm 0.04)\ M^{-1}\ s^{-1}$ (although the latter is not correctly predicted by the activation parameters reported in that work,

dx.doi.org/10.1021/ic401343m | *Inorg. Chem.* 2013, 52, 13904−13917

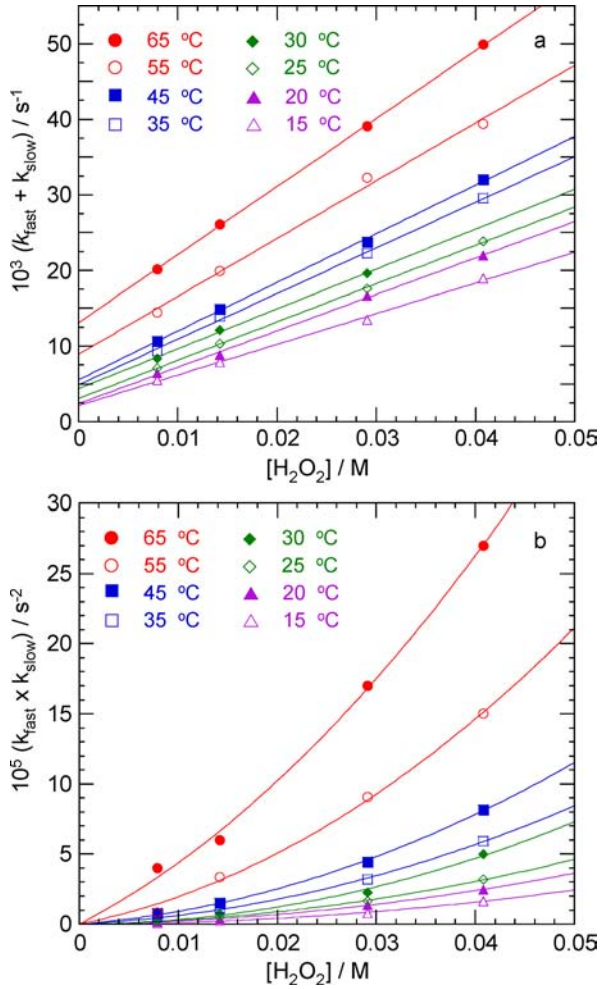

Figure 6. Dependence on excess [H_2O_2] of (a) the sum of the directly measured rate constants (k_{fast} + k_{slow}), showing curve-fits obtained using eq 14; and (b) the product of the directly measured rate constants (k_{fast} × k_{slow}), showing curve-fits obtained using eq 15, at eight different temperatures.

Table 3. Comparison of Experimental and Computed Rate and Equilibrium Constants for the Reversible Formation of A and B, via the Reactions of MTO with H_2O_2 in Acetonitrile Containing 2.0 M H_2O at 25 °C

	experimental		calculated
parameter	ref 32	this work[a]	this work
10^3 k_1 (M^{-1} s^{-1})	810(40)	471.4(63)	18
10^3 k'_{-1} (s^{-1})	3.9(2)[b]	2.84(16)	24
10^3 k_2 (M^{-1} s^{-1})	45(2)	34.7(20)	0.61
10^3 k_{-2} (s^{-1})	0.068(7)[b]	0.224(72)	1.4
K'_1 (M^{-1})	209(6)[c]	162(23)[d]	0.75
K_2 (M^{-1})	660(64)[c]	114(19)[d]	0.45

[a]Uncertainties are shown in parentheses. Extra significant figures are provided to facilitate interconversion of thermodynamic parameters, as recommended in ref 104. [b]Previously published values of the reverse rate constants were calculated as $k'_{-1} = k_1/K'_1$ and $k_{-2} = k_2/K_2$. [c]On the basis of a single-temperature measurement at 25 °C. [d]K'_1 and K_2 were calculated from the experimentally determined free energies, Table 1.

suggesting instead that k_1 should be much smaller, ca. 3×10^{-3} M^{-1} s^{-1}).[32] Our experimentally determined values of k_{-1} and k_2 more closely resemble previously published values,[32,33] while our value of k_{-2} is larger than the published value.

It is also possible to measure the kinetics of peroxo complex formation using ^{1}H NMR spectroscopy, although higher concentrations of MTO (ca. 13.0 mM, compared to 1.0 mM used in the UV−vis experiments) were required to obtain good signal-to-noise ratios. The time-dependence of the NMR signals is described by equations analogous to eqs 3 and 4. The observed rate constants k_{fast} and k_{slow} obtained in this way are similar to those measured by UV−vis spectrophotometry (Table S7, Supporting Information).

The experimentally measured values of both forward rate constants are ca. 160× larger than the corresponding reverse rate constants at 25.0 °C, Table 3). The computed values of k_1 and k_2 are 2 orders of magnitude smaller than the experimental values, which we nevertheless consider to be good agreement since the differences correspond to modest $\Delta\Delta G^{\ddagger}$ values of only 5−10 kJ mol^{-1}, within the typical error of modern DFT methods (which could be 15 kJ mol^{-1} or more).[75] The agreement is even better for k'_{-1} and k_{-2}: both computed values are within an order of magnitude of the corresponding experimental numbers.

Thermodynamics of Sequential Formation of A and B. The forward and reverse rate constants are related by the equilibrium relationships in eqs 16 and 17:

$$K_1 = \frac{[\mathbf{A}][H_2O]}{[MTO][H_2O_2]} = \frac{k_1}{k'_{-1}}[H_2O] = K'_1[H_2O] \quad (16)$$

$$K_2 = \frac{[\mathbf{B}]}{[\mathbf{A}][H_2O_2]} = \frac{k_2}{k_{-2}} \quad (17)$$

Van't Hoff plots were constructed from the ratios $K_1 = k_1[H_2O]/k'_{-1}$ and $K_2 = k_2/k_{-2}$ at each temperature, Figure 7. From the slopes ($-\Delta H_i/R$) and intercepts ($\Delta S_i/R$), and using full statistical error propagation to estimate the uncertainties,[111] we obtain $\Delta G_1 = (-14.3 \pm 4.2)$ kJ mol^{-1} and $\Delta G_2 = (-11.7 \pm 2.6)$ kJ mol^{-1}, both at 25.0 °C. We note that our experimental

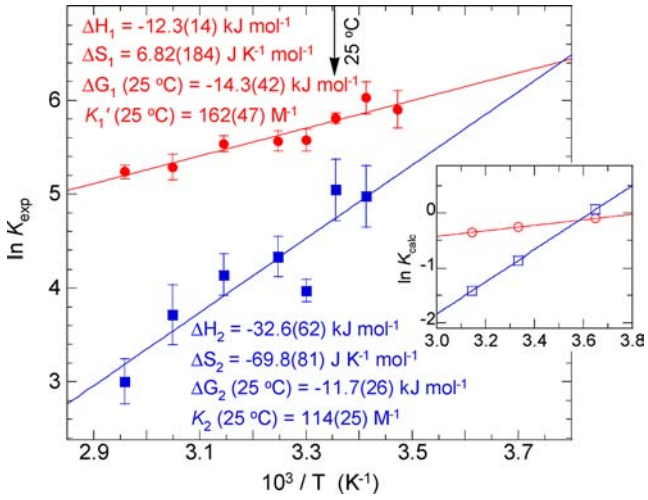

Figure 7. Van't Hoff plots, showing thermodynamic parameters obtained using the forward and reverse rate constants measured for formation of **A** (red) and **B** (blue) from MTO and H_2O_2 in CH_3CN containing 2.0 M H_2O. The extrapolated equilibrium constants are equal at 264.5 K. The inset shows the comparable van't Hoff plots made using the computed rate constants.

dx.doi.org/10.1021/ic401343m | Inorg. Chem. 2013, 52, 13904−13917

finding $\Delta G_1 < \Delta G_2$ at this temperature agrees with our computational prediction (Table 1).

The values of our experimentally derived thermodynamic parameters are summarized in Table 1. The measured values $\Delta H_1 = -12.3$ kJ mol^{-1} and $\Delta S_1 = 6.8$ J K^{-1} mol^{-1} are both small, while $\Delta H_2 = -32.8$ kJ mol^{-1} and $\Delta S_2 = -70.6$ J K^{-1} mol^{-1} have much larger magnitudes. The sequential formation constants K_1' and K_2 obtained from the experimental free energies are (162 ± 23) M^{-1} and (114 ± 19) M^{-1}, respectively, at 25.0 °C (Table 2). The single-temperature values for K_1' and K_2 (based solely on the measured values of the rate constants at 25.0 °C) are essentially the same: (166 ± 9) and (155 ± 51) M^{-1}, respectively, but with larger uncertainties.

Independent Experimental Evaluation of Equilibrium Constants. Our value of K_2 obtained using reaction kinetics is much smaller than a previously published value.[32] Therefore we sought to confirm it independently. In the earlier study, equilibrium constants were obtained from ^{1}H NMR spectra. One of our attempts to repeat this experiment is shown in Figure 8. The signal for MTO had almost disappeared by the time the first scan was recorded (4 min after H_2O_2 addition), and when the reaction mixture had reached equilibrium, the signal for **A** was very small. Thus it proved impossible to obtain very meaningful values for either equilibrium constant in this way. K_1' and K_2 were calculated in the time interval [0, 4] min and [24, 100] min, respectively, resulting in the values K_1' = (374 ± 181) M^{-1} and K_2 = (470 ± 344) M^{-1}. The small values of [MTO] at short times, and of [**A**] at long times are responsible for the large uncertainties.

An alternate method for measuring equilibrium constants relates the final UV–vis absorbance to the concentration of H_2O_2, using eq 7.[10,35] In solvent systems where $K_2 \gg K_1'$,[10,25,35] four curve-fit parameters can be allowed to vary independently: ε_A, ε_B, K_1', and K_2. However, convergence is problematic when $K_1' \approx K_2$, which our results indicate to be the case for aqueous CH_3CN near room temperature (see above). In order to evaluate equilibrium constants using eq 7, we therefore reduced the number of variables in the fit by determining the extinction coefficients $\varepsilon_{A,360}$ and $\varepsilon_{B,360}$ independently.

To measure $\varepsilon_{B,360}$, 1.0 mM MTO was added to CH_3CN containing 2.0 M H_2O at three different H_2O_2 concentrations (38.5, 60.0, and 100.0 mM) and 25.0 °C. After reaction, the final, stable absorbance at 360 nm was measured. For $[H_2O_2]_0 \gg [MTO]_0$, the equilibrium concentration of **B** is negligibly different from $[MTO]_0$. The resulting value of $\varepsilon_{B,360}$ (1148 ± 12) M^{-1} cm^{-1} is comparable to previously reported values in aqueous acetonitrile and water (1100–1200 M^{-1} cm^{-1}).[10,32] To obtain $\varepsilon_{A,360}$, the time-dependent concentrations of **A** and **B** were simulated, using the biexponential curve-fit parameters k_{fast} and k_{slow} obtained from our kinetics experiments. The value of $\varepsilon_{A,360}$ was then obtained as a function of time, using eq 18:

$$\varepsilon_{A,360} = (\mathrm{Abs}_{360,t} - [\mathbf{B}]_t \varepsilon_{B,360} l)/[\mathbf{A}]_t \quad (18)$$

where l is the path length. Once the ligand exchange reaction in eq 1 was quasi-equilibrated, the value of $\varepsilon_{A,360}$ remained constant at (392 ± 35) M^{-1} cm^{-1}. The stated uncertainty arises from averaging the results of multiple experiments using different $[H_2O_2]$. Comparable values (380–500 M^{-1} cm^{-1}) have been reported in acidic water.[10]

The final absorbance values and resulting curve-fit are shown in Figure 9, with the fitted values of K_1' and K_2. The resulting equilibrium constants are virtually the same (within experimental error) as the values obtained by kinetic analysis (although the latter are considerably more precise). The uncertainties are based on full statistical error propagation. The greater precision of the kinetics-based values is a consequence

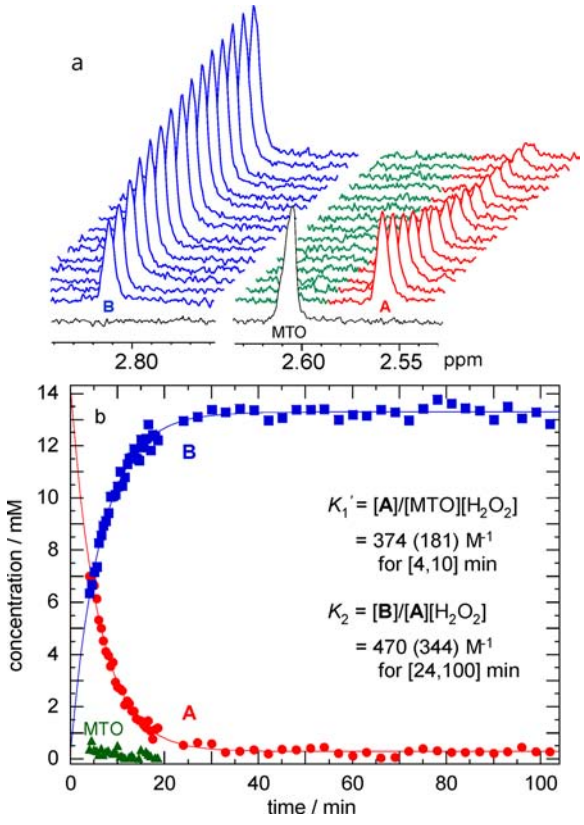

Figure 8. (a) ^{1}H NMR spectra recorded during the first 18 min of reaction between 13.0 mM MTO and 140.0 mM H_2O_2, at 27.0 °C in CD_3CN containing 2.6 M H_2O and 0.100 M $HClO_4$. The first spectrum (black) was collected before H_2O_2 addition. (b) Time-dependent concentration profiles extracted from the NMR spectra. The solid lines are the nonlinear least-squares curve-fits obtained using eqs 3 and 4.

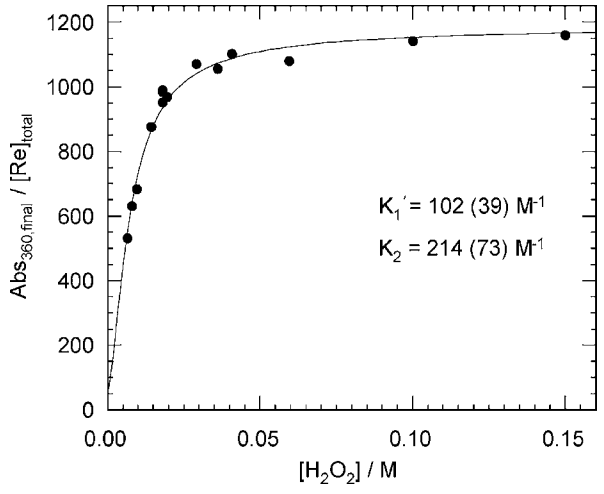

Figure 9. Dependence of the final absorbance at 360 nm (path length 1 cm) on excess $[H_2O_2]$, for solutions of 1.0 mM MTO in CH_3CN containing 2.0 M H_2O, at 25.0 °C. The solid line is the curve-fit using eq 7.

dx.doi.org/10.1021/ic401343m | Inorg. Chem. 2013, 52, 13904–13917

of the very good model provided by the curve-fit equations (seen in the quality of the fits in Figures 3 and 4), as well as the much greater number of independent experiments: 32, at four different H_2O_2 concentrations and eight different temperatures. For comparison, the equilibrium constants measured by ^1H NMR are the result of a single, highly imprecise experiment at a single temperature (Figure 8, reproducing the experiment reported in ref 32). The measurement of final UV−vis absorbance involved 13 independent experiments at 11 different H_2O_2 concentrations but all at a single temperature (as in previous work).

"Cooperativity" in peroxo ligand binding to MTO has been invoked in many solvent systems, including water,[10] ionic liquids,[35] and semiaqueous organic solvents such as methanol,[25,33] acetonitrile,[32,42] and nitromethane,[33] based on reported findings of $K_1'/K_2 \ll 1$ at 25.0 °C. Our results do not follow this trend: both experimentally and computationally, we find $K_1' > K_2$ near room temperature. The impact on the speciation of MTO in the presence of H_2O_2 is quite significant. In particular, Figure 10 shows that **A** is present in higher

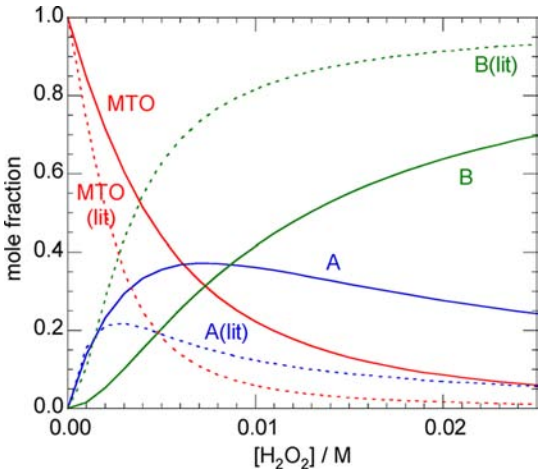

Figure 10. MTO speciation as a function of $[H_2O_2]$ in aqueous acetonitrile (containing 2.0 M H_2O) at 25.0 °C. Solid lines were calculated based on values for the equilibrium constants K_1' and K_2 measured in this work; dashed lines are based on previously reported values.[32]

concentrations and persists at much higher values of $[H_2O_2]$ than previously thought. This is important because, although both **A** and **B** are competent catalysts in selective oxidations,[4,17] they have different stabilities in the presence of H_2O and H_2O_2, and decompose via different pathways.[13,32,33]

Furthermore, since the equilibrium constants have very different temperature dependences (Figure 7), the ratio (K_1'/K_2) increases dramatically with temperature. The value of K_1' is less than K_2 in aqueous CH_3CN only at low temperatures (below ca. −10 °C, according to Figure 7). Similar temperature dependences are evident for the calculated equilibrium constants based on our computed rate constants (Figure 7, inset).

Experimental Activation Parameters. The temperature dependence of the pseudo-second-order rate constants k_1 and k_2 was used to obtain apparent activation parameters for the formation of **A** and **B**, via the Eyring plots shown in Figure 11a,b. The resulting values of $\Delta H_1^{\ddagger}$ and $\Delta S_1^{\ddagger}$ are (8.4 ± 0.7) kJ mol^{-1} and −(223 ± 1) J K^{-1} mol^{-1}, respectively. Our very

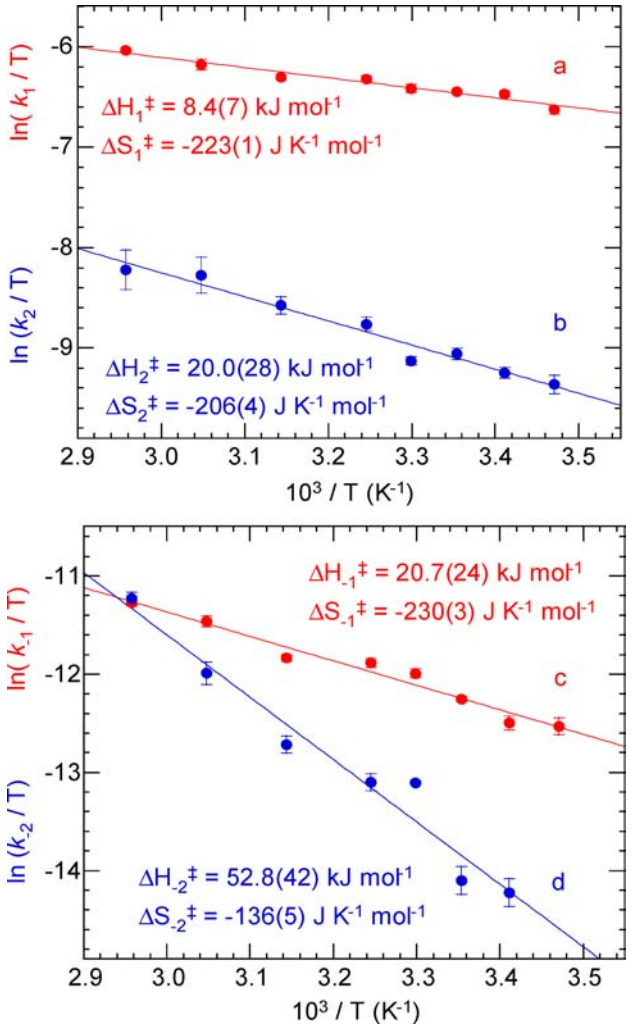

Figure 11. Eyring plots for each of the experimentally measured H_2O_2-independent rate constants involved in the formation of peroxo complexes **A** and **B**. In (c), the pseudo-first-order rate constant k_{-1}' was divided by $[H_2O]$ to satisfy the requirements of microscopic reversibility and to allow calculation of ΔH_1 and ΔS_1 as the difference in the corresponding activation parameters for the forward and reverse reactions.

small value of $\Delta H_1^{\ddagger}$ suggests highly concerted bond-breaking and bond-making in the transition state leading to **A**, while the large negative value of $\Delta S_1^{\ddagger}$, −223 J K^{-1} mol^{-1}, indicates a highly structured transition state as predicted computationally for the water-catalyzed mechanism. Consequently, the free energy barrier at room temperature is predominantly entropic.

Activation parameters corresponding to the conversion of **A** to **B** are given in Table 5. Our value for $\Delta H_2^{\ddagger}$, (20.0 ± 2.8) kJ mol^{-1}, is much larger than $\Delta H_1^{\ddagger}$, (8.4 ± 0.7) kJ mol^{-1}. The values of $\Delta S_1^{\ddagger}$ and $\Delta S_2^{\ddagger}$ are very similar, suggesting a close resemblance in their highly structured transition states. The slower formation of **B** relative to **A** is therefore a consequence of a much larger enthalpic barrier.

Eyring analyses for the reverse reactions, that is, the reversion of **B** to **A**, and the hydrolysis of **A** to give MTO, are conducted here for the first time, Figure 11c,d. The resulting activation parameters are shown in Tables 4 and 5. Combining values for the forward and reverse reactions yields values for ΔH_1 and ΔS_1 of (−12.3 ± 1.8) kJ mol^{-1} and (6.8 ± 0.1) J K^{-1} mol^{-1}, respectively, corresponding to ΔG_1 = (−14.3 ± 2.1) kJ mol^{-1}

dx.doi.org/10.1021/ic401343m | Inorg. Chem. 2013, 52, 13904−13917

Table 4. Comparison of Experimental and Computed Activation Parameters for the Reversible Formation of $CH_3ReO_2(\eta^2\text{-}O_2)$, A, via the Reaction of MTO with H_2O_2 in CH_3CN with 2 M H_2O

	experimental		calculated
parameter[a]	ref 32	this work[b]	this work
$\Delta H_1^{\ddagger}$	24.5(1.9)[c]	8.38(73)	31
$\Delta S_1^{\ddagger}$	−212(6)	−223.18(95)	−175
$\Delta G_1^{\ddagger}$	87.7(38)	74.92(655)	83
$\Delta H_{-1}^{\ddagger}$	*d*	20.69(235)	35
$\Delta S_{-1}^{\ddagger}$	*d*	−229.98(303)	−164
$\Delta G_{-1}^{\ddagger}$	86.7(1)	89.26(1022)	84

[a]Enthalpies and free energies are reported in kJ mol^{-1}, entropies in J K^{-1} mol^{-1}. Free energies correspond to 25.0 °C. [b]Parameters were extracted from the Eyring plots in Figure 11. Uncertainties, shown in parentheses, were calculated by full statistical error propagation of the Eyring equation.[111] Extra significant figures are provided to facilitate interconversion of thermodynamic parameters, as recommended in ref 104. [c]The earlier Eyring analysis appears to have been conducted using pseudo-first-order values of k_{fast}, measured for different values of excess $[H_2O_2]$.[32] [d]The activation enthalpy and entropy for the reverse reaction were not reported.

Table 5. Comparison of Experimental and Computed Activation Parameters for the Reversible Formation of $CH_3ReO(\eta^2\text{-}O_2)_2(H_2O)$, B, by the reaction of $CH_3ReO_2(\eta^2\text{-}O_2)$, A, with H_2O_2 in CH_3CN with 2 M H_2O

	experimental		calculated
parameter[a]	ref 32	this work[b]	this work
$\Delta H_2^{\ddagger}$	29.0(7)	19.98(275)	39
$\Delta S_2^{\ddagger}$	−214(2)	−206.21(354)	−176
$\Delta G_2^{\ddagger}$	92.8(13)	81.46(1130)	91
$\Delta H_{-2}^{\ddagger}$	*c*	52.80(423)	63
$\Delta S_{-2}^{\ddagger}$	*c*	−135.61(546)	−88
$\Delta G_{-2}^{\ddagger}$	96.8(3)	93.23(837)	89

[a]Enthalpies and free energies are reported in kJ mol^{-1}, entropies in J K^{-1} mol^{-1}. Free energies correspond to 25.0 °C. [b]Parameters were extracted from the Eyring plots in Figure 11. Uncertainties, shown in parentheses, were calculated by full error propagation of the Eyring equation.[111] Extra significant figures are provided to facilitate interconversion of thermodynamic parameters, as recommended in ref 104. [c]The activation enthalpy and entropy for the reverse reaction were not reported.

and, consequently, $K_1' = (162 \pm 23)$, at 25.0 °C. Using a similar approach, we obtain values for ΔH_2 and ΔS_2 of (-32.8 ± 5.2) kJ mol^{-1} and (-70.6 ± 3.1) J K^{-1} mol^{-1}, respectively, leading to $\Delta G_2 = (-11.8 \pm 1.9)$ kJ mol^{-1} and $K_2 = (114 \pm 19)$ at 25.0 °C. The Eyring and van't Hoff approaches give consistent results (as expected, since they are based on the same data). However, the Eyring analyses yield much smaller uncertainties for thermodynamic parameters involving formation of **B**. Consequently, these are the values we choose to present in Table 1.

Comparison of the experimental activation parameters for each of the four ligand exchange reactions reveals interesting trends. The activation enthalpies for the conversion of MTO to **A**, of **A** to **B**, as well as the reversion of **A** to MTO, are all small ($\leq$20 kJ mol^{-1}), but the activation enthalpy for reversion of **B** to **A** is significantly larger (53 kJ mol^{-1}). At the same time, the activation entropies are all ca. −200 J K^{-1} mol^{-1}, except for reversion of **B** to **A** (−135 J K^{-1} mol^{-1}). The same trends are present in the computed values. The similarities in activation parameters for the two forward steps are readily understood: according to our computational model both involve association of three components (the transition metal species, H_2O_2, and H_2O). Reversion of **A** to MTO also requires association of three components: the transition metal species and *two* H_2O molecules. Bond formation partially compensates for bond-breaking, reducing the activation enthalpy in each case. In contrast, reversion of **B** to **A** involves relatively more bond-breaking, according to our computational model since only two species are required to associate: the transition metal complex and one water molecule. The second water molecule, which is already coordinated to **B**, must dissociate in the transition state. This accounts for both the higher $\Delta H_{-2}^{\ddagger}$ and the less negative $\Delta S_{-2}^{\ddagger}$.

The good agreement between calculated and experimental activation entropies results in reasonably close computed and experimental rate constants, despite calculated activation enthalpies that are too large for eq 1 (forward and reverse directions) and eq 2 (forward direction only). This reflects the dominance of the entropy term in the free energy barriers. In view of our confidence in the computationally predicted water-catalyzed mechanism, inspired by the detailed comparisons with experimental kinetics as described above, we sought experimental evidence for the direct involvement of water in the ligand exchange reactions.

Water Acceleration of Experimental Ligand Exchange Kinetics. The pseudo-second-order rate constants k_1 and k_2 for the sequential reactions of MTO with H_2O_2 are highly solvent-dependent. Both have been reported to be ca. 100 times faster in pure H_2O[10] than in either methanol[33] or acetonitrile,[32] and up to 1000 times faster than in nitromethane[33] (all containing some water, which inevitably enters with the aqueous H_2O_2 reagent). To confirm our computational prediction of a direct role for water in ligand exchange, we undertook a preliminary experimental evaluation of the kinetic dependence on water.

The reaction between 1.0 mM MTO and 18.0 mM H_2O_2 was studied at 25.0 °C in CH_3CN in the presence of variable amounts of water, up to 4.0 M. The kinetic profiles were analyzed as described above, and the resulting rate constants are shown in Table S9, Supporting Information. Figure 12 shows that both pseudo-first-order rate constants increase rapidly with increasing $[H_2O]$, consistent with direct involvement of water in the transition states. The acceleration is significantly greater for k_{fast} than for k_{slow}. Owens and Abu-Omar reported that k_2 varies linearly with $[H_2O]$ in various ionic liquids.[35]

These measurements support our computational finding of a water-catalyzed mechanism. However, detailed analysis of the water dependence of the experimental rate law is complicated by the reversibility of the reactions, differences in their reaction orders with respect to H_2O, as well as the highly nonideal nature of acetonitrile−water mixtures.[112] Water activity coefficients are significantly greater than unity,[113] enhancing the nonlinearity in the variation of the rate constants with $a(H_2O)$, relative to $[H_2O]$. The common practice of deducing the reaction order with respect to water directly from the $[H_2O]$-dependence of its rate constant is inadequate here.

The heterogeneous microstructure of this solvent mixture consists of H-bonded clusters of several water molecules associated with a much smaller number of acetonitrile molecules.[114−116] Microsolvation of the various Re complexes is expected to change dramatically with $[H_2O]$ as the number

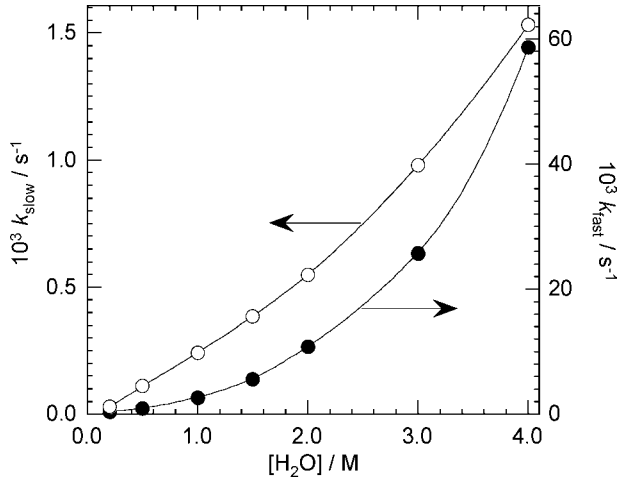

Figure 12. Dependence of the measured pseudo-first-order rate constants k_{fast} (solid circles) and k_{slow} (open circles) on the nominal water concentration, for the reaction of 1.0 mM MTO with 18.0 mM H_2O_2, in aqueous CH_3CN at 25.0 °C. Lines are drawn only to guide the eye.

and size of the water clusters changes. Consequently, we defer a full analysis of the role of water in the rate law to a future report. Nevertheless, the details of this water effect are likely responsible for some of the remaining discrepancies between our computed and experimental rate constants.

CONCLUSIONS

Activation of H_2O_2 by ligand exchange is a key (possibly even rate-determining) step in selective oxidation reactions catalyzed by transition metal complexes.[117−119] Previous studies of the kinetics and thermodynamics of H_2O_2 activation by MTO contain many inconsistencies. Here we provide a better understanding of these reactions and consistent experimental data for benchmarking future computational studies of MTO and its derivatives. Our computational model is the first to correctly predict negative reaction enthalpies for each reaction, and the first to correctly predict the hydration states for **A** and **B** in aqueous CH_3CN. We also provide the first calculation of the forward and reverse rate constants as a function of temperature, using density functional theory and including tunneling and solvation contributions to the free energy. Forward and reverse rate constants and equilibrium constants were also measured experimentally. Interestingly, the equilibrium constants do not confirm the strong co-operativity of peroxide ligand binding reported previously. Computation of rate constants predicts a water-catalyzed mechanism that is at least 7 orders of magnitude faster than direct ligand exchange. In this first direct comparison of computed and observed rate constants, we find reasonable agreement. Moreover, experiments confirm our computational prediction that the rate of each step should increase with water concentration.

The evidence for water-catalyzed H_2O_2 activation by MTO may have mechanistic implications in olefin epoxidation, which are reported to be an order of magnitude faster when organic solvents are made semiaqueous[17,120] (although the opposite effect has been reported for perfluorinated solvents).[121] For most catalysts, protonation of an η^2-peroxo ligand yields an η^1-hydroperoxide that is much more reactive because of its greater electrophilicity.[110,122] However, for MTO the η^2-peroxo forms are predicted to be more active,[123] making it possible that the water acceleration observed in olefin epoxidation arises due to the ligand exchange process.

ASSOCIATED CONTENT

Supporting Information

Observed values of all experimental rate constants; individual contributions to the total free energies of ground states, water-free and water-assisted transition states; basis set, imaginary frequencies and tunneling corrections; energies and Cartesian coordinates of all computed structures comparison of computed activation parameters with and without tunneling; comparison of computed thermodynamic parameters from van't Hoff plot and from partition functions; extra significant figures for all computed rate constants, activation parameters, and thermodynamic parameters; detailed description of calculation for solution-phase free energies. This material is available free of charge via the Internet at http://pubs.acs.org.

AUTHOR INFORMATION

Corresponding Authors

*(B.P.) E-mail: baronp@engineering.ucsb.edu.
*(S.L.S.) E-mail: sscott@engineering.ucsb.edu.

Notes

The authors declare no competing financial interest.
#T.H. and B.R.G. contributed equally to this work.

ACKNOWLEDGMENTS

T.H. is grateful to Air Products for a graduate fellowship. B.R.G. acknowledges the PIRE-ECCI program (NSF-OISE 0530268) for a graduate fellowship. The authors thank S. M. Stewart for useful input on the choice of basis sets and core potentials, and V. Agarwal for advice on using the solvation entropy correction. This work was funded by the Catalysis Science Initiative of the U.S. Department of Energy, Basic Energy Sciences (DE-FG02-03ER15467).

REFERENCES

(1) Köstlmeier, S.; Nasluzov, V. A.; Herrmann, W. A.; Rösch, N. *Organometallics* **1997**, *16*, 1786.
(2) Gisdakis, P.; Antonczak, S.; Köstlmeier, S.; Herrmann, W. A.; Rösch, N. *Angew. Chem., Int. Ed.* **1998**, *37*, 2211 Optimizations were performed using B3LYP/LanL2DZ on Re and 6-311G(d,p) on H, C, and O, followed by single-point energy calculations, with a (441/2111/21/11) decontracted LanL2DZ basis set where two f-type exponents (0.5895 and 0.2683) were added on Re.
(3) Pietsch, M. A.; Russo, T. V.; Murphy, R. B.; Martin, R. L.; Rappé, A. K. *Organometallics* **1998**, *17*, 2716.
(4) Espenson, J. H. *Chem. Commun.* **1999**, 479.
(5) Gisdakis, P.; Rösch, N.; Bencze, É.; Mink, J.; Gonçalves, I. S.; Kühn, F. E. *Eur. J. Inorg. Chem.* **2001**, 981.
(6) Morris, L. J.; Downs, A. J.; Greene, T. M.; McGrady, G. S.; Herrmann, W. A.; Sirsch, P.; Scherer, W.; Gropen, O. *Organometallics* **2001**, *20*, 2344.
(7) de Simone, M.; Coreno, M.; Green, J. C.; McGrady, S.; Pritchard, H. *Inorg. Chem.* **2003**, *42*, 1908.
(8) Costa, P. J.; Calhorda, M. J.; Bossert, J.; Daniel, C.; Romão, C. C. *Organometallics* **2006**, *25*, 5235.
(9) Gonzales, J. M.; Distasio, R., Jr.; Periana, R. A.; Goddard, W. A., III.; Oxgaard, J. *J. Am. Chem. Soc.* **2007**, *129*, 15794 Model chemistry: CPCM-optimized-B3LYP/6-311G**++//B3LYP/6-311G**.
(10) Yamazaki, S.; Espenson, J. H.; Huston, P. *Inorg. Chem.* **1993**, *32*, 4683.
(11) Espenson, J. H.; Pestovsky, O.; Huston, P.; Staudt, S. *J. Am. Chem. Soc.* **1994**, *116*, 2869.
(12) Hansen, P. J.; Espenson, J. H. *Inorg. Chem.* **1995**, *34*, 5839.

(13) Abu-Omar, M. M.; Hansen, P. J.; Espenson, J. H. *J. Am. Chem. Soc.* **1996**, *118*, 4966.
(14) Herrmann, W. A.; Wagner, W.; Flessner, U. N.; Volkhardt, U.; Komber, H. *Angew. Chem., Int. Ed.* **1991**, *30*, 1636.
(15) Moses, A. W.; Raab, C.; Nelson, R. C.; Leifeste, H. D.; Ramsahye, N. A.; Chattopadhyay, S.; Eckert, J.; Chmelka, B. F.; Scott, S. L. *J. Am. Chem. Soc.* **2007**, *129*, 8912.
(16) Moses, A. W.; Ramsahye, N. A.; Raab, C.; Leifeste, H. D.; Chattopadhyay, S.; Chmelka, B. F.; Eckert, J.; Scott, S. L. *Organometallics* **2006**, *25*, 2157.
(17) Kühn, F. E.; Scherbaum, A.; Herrmann, W. A. *J. Organomet. Chem.* **2004**, *689*, 4149.
(18) Herrmann, W. A.; Wang, M. *Angew. Chem., Int. Ed.* **1991**, *30*, 1641.
(19) Herrmann, W. A.; Roesky, P. W.; Wang, M.; Scherer, W. *Organometallics* **1994**, *13*, 4531.
(20) Owens, G. S.; Arias, J.; Abu-Omar, M. M. *Catal. Today* **2000**, *55*, 317.
(21) Santos, A. M.; Pedro, F. M.; Yogalekar, A. A.; Lucas, I. S.; Romão, C. C.; Kühn, F. E. *Chem.—Eur. J.* **2004**, *10*, 6313.
(22) Herrmann, W. A.; Fischer, R. W.; Marz, D. W. *Angew. Chem., Int. Ed.* **1991**, *30*, 1638.
(23) Vassell, K. A.; Espenson, J. H. *Inorg. Chem.* **1994**, *33*, 5491.
(24) Al-Ajlouni, A. M.; Espenson, J. H. *J. Am. Chem. Soc.* **1995**, *117*, 9243.
(25) Zhu, Z.; Espenson, J. H. *J. Org. Chem.* **1995**, *60*, 1326.
(26) Ziegler, J. E.; Zdilla, M. J.; Evans, A. J.; Abu-Omar, M. M. *Inorg. Chem.* **2009**, *48*, 9998.
(27) Ahmad, I.; Chapman, G.; Nicholas, K. M. *Organometallics* **2011**, *30*, 2810.
(28) Yi, J.; Liu, S.; Abu-Omar, M. M. *ChemSusChem* **2012**, *5*, 1401.
(29) Shiramizu, M.; Toste, F. D. *Angew. Chem., Int. Ed.* **2012**, *51*, 8082.
(30) Schuchardt, U.; Mandelli, D.; Shul'pin, G. B. *Tetrahedron Lett.* **1996**, *37*, 6487.
(31) Kirillova, M. V.; Kirillov, A. M.; Reis, P. M.; Silva, J. A. L.; Fraústo da Silva, J. J. R.; Pombeiro, A. J. L. *J. Catal.* **2007**, *248*, 130.
(32) Wang, W. D.; Espenson, J. H. *Inorg. Chem.* **1997**, *36*, 5069.
(33) Wang, W. D.; Espenson, J. H. *J. Am. Chem. Soc.* **1998**, *120*, 11335.
(34) Kühn, F. E.; Herrmann, W. A. In *Aqueous-Phase Organometallic Catalysis*; 2nd ed.; Cornils, B., Herrmann, W. A., Eds.; Wiley-VCH: Weinheim, 2004; p 488.
(35) Owens, G. S.; Abu-Omar, M. M. *J. Mol. Catal. A: Chem.* **2002**, *187*, 215.
(36) Crucianelli, M.; Saladino, R.; De Angelis, F. *ChemSusChem* **2010**, *3*, 524.
(37) Campos-Martin, J. M.; Blanco-Brieva, G.; Fierro, J. L. G. *Angew. Chem., Int. Ed.* **2006**, *45*, 6962.
(38) Blackmond, D. G.; Armstrong, A.; Coombe, V.; Wells, A. *Angew. Chem., Int. Ed.* **2007**, *46*, 3798.
(39) Ghanta, M.; Ruddy, T.; Fahey, D.; Busch, D.; Subramaniam, B. *Ind. Eng. Chem. Res.* **2012**, *52*, 18.
(40) Herrmann, W. A.; Fischer, R. W.; Scherer, W.; Rauch, M. U. *Angew. Chem., Int. Ed.* **1993**, *32*, 1157.
(41) Pestovsky, O.; van Eldik, R.; Huston, P.; Espenson, J. H. *Dalton Trans.* **1995**, 133.
(42) Abu-Omar, M. M.; Espenson, J. H. *J. Am. Chem. Soc.* **1995**, *117*, 272.
(43) Kuznetsov, M. L.; Pombeiro, A. J. L. *Inorg. Chem.* **2008**, *48*, 307 Computational method: CPCM-B3LYP/6-311G(d,p)//gas-B3LYP/6-31G(d).
(44) Valentin, C. D.; Gandolfi, R.; Gisdakis, P.; Rösch, N. *J. Am. Chem. Soc.* **2001**, *123*, 2365 Model chemistry: Optimizations with B3LYP/LanL2DZ (with 6-311G(d,p) for main group elements). Energies of stationary points were then refined in single-point fashion by augmenting the Re basis set by two f-type polarization exponents (0.5895 and 0.2683) and using the basis set 6-311+G(d,p) for main group elements.
(45) Karlsson, E. A.; Privalov, T. *Chem.—Eur. J.* **2009**, *15*, 1862 Model chemistry: PB-SCRF/PCM.
(46) Herrmann, W. A.; Kuchler, J. G.; Weichselbaumer, G.; Herdtweck, E.; Kiprof, P. *J. Org. Chem.* **1989**, *372*, 351.
(47) Breslow, R. *Acc. Chem. Res.* **1991**, *24*, 159.
(48) Butler, R. N.; Coyne, A. G. *Chem. Rev.* **2010**, *110*, 6302.
(49) Raj, M.; Singh, V. K. *Chem. Commun.* **2009**, *0*, 6687.
(50) Kandori, H.; Yamazaki, Y.; Sasaki, J.; Maeda, A.; Needleman, R.; Lanyi, J. K. *J. Am. Chem. Soc.* **1995**, *117*, 2118.
(51) Wang, L.; Yu, X.; Hu, P.; Broyde, S.; Zhang, Y. *J. Am. Chem. Soc.* **2007**, *129*, 4731.
(52) Lutz, S.; Tubert-Brohman, I.; Yang, Y.; Meuwly, M. *J. Biol. Chem.* **2011**, *286*, 23679.
(53) Vilotijevic, I.; Jamison, T. F. *Science* **2007**, *317*, 1189.
(54) Morokuma, K.; Muguruma, C. *J. Am. Chem. Soc.* **1994**, *116*, 10316.
(55) Nguyen, M. T.; Raspoet, G.; Vanquickenborne, L. G.; Van Duijnen, P. T. *J. Phys. Chem. A* **1997**, *101*, 7379.
(56) Loerting, T.; Liedl, K. R. *J. Phys. Chem. A* **2001**, *105*, 5137.
(57) Vöhringer-Martinez, E.; Hansmann, B.; Hernandez, H.; Francisco, J. S.; Troe, J.; Abel, B. *Science* **2007**, *315*, 497.
(58) Koch, D. M.; Toubin, C.; Peslherbe, G. H.; Hynes, J. T. *J. Phys. Chem. C* **2008**, *112*, 2972.
(59) Ryder, J. A.; Chakraborty, A. K.; Bell, A. T. *J. Phys. Chem. B* **2000**, *104*, 6998.
(60) Blaszkowski, S. R.; van Santen, R. A. *J. Am. Chem. Soc.* **1997**, *119*, 5020.
(61) Rozanska, X.; van Santen, R. A. In *Handbook of Zeolite Science and Technology*; Auerbach, S. M., Carrado, K. A., Dutta, P. K., Eds.; Dekker: New York, 2003; pp 1000−1058.
(62) Seshadri, V.; Westmoreland, P. R. *J. Phys. Chem. A* **2012**, *116*, 11997.
(63) Lim, C.-H.; Holder, A. M.; Musgrave, C. B. *J. Am. Chem. Soc.* **2012**, *135*, 142.
(64) Shi, F.-Q.; Li, X.; Xia, Y.; Zhang, L.; Yu, Z.-X. *J. Am. Chem. Soc.* **2007**, *129*, 15503.
(65) Ohnishi, Y.-Y.; Nakao, Y.; Sato, H.; Sakaki, S. *Organometallics* **2006**, *25*, 3352.
(66) Bianco, R.; Hay, P. J.; Hynes, J. T. *J. Phys. Chem. A* **2011**, *115*, 8003.
(67) Frisch, M. J.; Trucks, G. W.; Schlegel, H. B.; Scuseria, G. E.; Robb, M. A.; Cheeseman, J. R.; Zakrzewski, V. G.; Montgomery, J. A., Jr.; Stratmann, R. E.; Burant, J. C.; Dapprich, S.; Millam, J. M.; Daniels, A. D.; Kudin, K. N.; Strain, M. C.; Farkas, O.; Tomasi, J.; Barone, V.; Cossi, M.; Cammi, R.; Mennucci, B.; Pomelli, C.; Adamo, C.; Clifford, S.; Ochterski, J.; Peterson, G. A.; Ayala, P. Y.; Cui, Q.; Morokuma, K.; Malick, D. K.; Rabuck, A. D.; Raghavachari, K.; Foresman, J. B.; Cioslowski, J.; Ortiz, J. V.; Baboul, A. G.; Stefanov; B. B.; Liu, G.; Liashenko, A.; Piskorz, P.; Komaromi, I.; Gomperts; R.; Martin, R. L.; Fox, D. J.; Keith, T.; Al-Laham, M. A.; Peng, C. Y.; Nanayakkara, A.; Challacombe, M.; Gill, P. M. W.; Johnson, B. C.; W.; Wong, M. W.; Andres, J. L.; Gonzalez, C.; Head-Gordon, M.; Replogle, E. S.; Pople, J. A. *Gaussian 09*; Gaussian, Inc.: Wallingford CT, 2009.
(68) Hay, P. J.; Wadt, W. R. *J. Phys. Chem.* **1985**, *82*, 270.
(69) Andrae, D.; Häußermann, U.; Dolg, M.; Stoll, H.; Preuß, H. *Theor. Chem. Acc.* **1990**, *77*, 123.
(70) Wadt, W. R.; Hay, P. J. *J. Chem. Phys.* **1985**, *82*, 284.
(71) Gisdakis, P.; Antonczak, S.; Rösch, N. *Organometallics* **1999**, *18*, 5044.
(72) Chai, J.-D.; Head-Gordon, M. *Phys. Chem. Chem. Phys.* **2008**, *10*, 6615.
(73) Zhao, Y.; Truhlar, D. G. *Theor. Chem. Acc.* **2008**, *120*, 215.
(74) Burke, K. *J. Chem. Phys.* **2012**, *136*, 150901.
(75) Zhao, Y.; Truhlar, D. G. *J. Chem. Theory Comput.* **2012**, *7*, 669.
(76) Yang, K.; Zheng, J.; Zhao, Y.; Truhlar, D. G. *J. Chem. Phys.* **2010**, *132*, 164117.
(77) Schenker, S.; Schneider, C.; Tsogoeva, S. B.; Clark, T. *J. Chem. Theory Comput.* **2011**, *7*, 3586.

(78) Minenkov, Y.; Singstad, Å.; Occhipinti, G.; Jensen, V. R. *Dalton Trans.* **2012**, *41*, 5526.
(79) Schuchardt, K. L.; Didier, B. T.; Elsethagen, T.; Sun, L.; Gurumoorthi, V.; Chase, J.; Li, J.; Windus, T. L. *J. Chem. Inf. Model.* **2007**, *47*, 1045.
(80) Feller, D. *J. Comput. Chem.* **1996**, *17*, 1571.
(81) Hay, P. J.; Wadt, W. R. *J. Chem. Phys.* **1985**, *82*, 299.
(82) Roy, L. E.; Hay, P. J.; Martin, R. L. *J. Chem. Theory Comput.* **2008**, *4*, 1029.
(83) Figgen, D.; Peterson, K. A.; Dolg, M.; Stoll, H. *J. Chem. Phys.* **2009**, *130*, 164108.
(84) Jensen, F. *Introduction to Computational Chemistry*, 2nd ed.; Wiley: Chichester, 2007.
(85) Wertz, D. H. *J. Am. Chem. Soc.* **1980**, *102*, 5316.
(86) Barone, V.; Cossi, M. *J. Phys. Chem. A* **1998**, *102*, 1995.
(87) Cossi, M.; Rega, N.; Scalmani, G.; Barone, V. *J. Comput. Chem.* **2003**, *24*, 669.
(88) Takano, Y.; Houk, K. N. *J. Chem. Theory Comput.* **2005**, *1*, 70.
(89) Baker, J. *J. Comput. Chem.* **1986**, *7*, 385.
(90) Cerjan, C.; Miller, W. *J. Chem. Phys.* **1981**, *75*, 2800.
(91) Banerjee, A.; Adams, N.; Simons, J.; Shepard, R. *J. Phys. Chem.* **1985**, *89*, 52.
(92) Eyring, H. *J. Chem. Phys.* **1935**, *3*, 107.
(93) Shavitt, I. *J. Chem. Phys.* **1959**, *31*, 1359.
(94) Gonzales-Lafont, A.; Truong, T. N.; Truhlar, D. G. *J. Chem. Phys.* **1991**, *95*, 8875.
(95) Peters, B.; Bell, A. T.; Chakraborty, A. *J. Chem. Phys.* **2004**, *121*, 4461.
(96) Skodje, R. T.; Truhlar, D. G.; Garrett, B. C. *J. Chem. Phys.* **1982**, *77*, 5955.
(97) Skodje, R. T.; Truhlar, D. G.; Garrett, B. C. *J. Phys. Chem.* **1981**, *85*, 3019.
(98) Laidler, K. J. *Chemical Kinetics*; Harper & Row: New York, 1987.
(99) Florian, J.; Warshel, A. *J. Phys. Chem. B* **1997**, *101*, 5583.
(100) Tomasi, J.; Mennucci, B.; Cammi, R. *Chem. Rev.* **2005**, *105*, 2999.
(101) Cramer, C. J.; Truhlar, D. G. *Acc. Chem. Res.* **2008**, *41*, 760.
(102) Klamt, A. *J. Phys. Chem.* **1995**, *99*, 2224.
(103) Klamt, A.; Jonas, V.; Bürger, T.; Lohrenz, J. C. W. *J. Phys. Chem. A* **1998**, *102*, 5074.
(104) Espenson, J. H. *Chemical Kinetics and Reaction Mechanisms*; 2nd ed.; McGraw-Hill: New York, 1995; pp 70−95.
(105) Herrmann, W. A.; Correia, J. D. G.; Artus, G. R. J.; Fischer, R. W.; Romão, C. C. *J. Organomet. Chem.* **1996**, *520*, 139.
(106) Formosinho, S. J.; Csizmadia, I. G.; Arnaut, L. G. *Theoretical and Computational Models for Organic Chemistry*; Kluwer Academic Publishers: Dordrecht, 1991.
(107) Steinfeld, J. I.; Francisco, J. S.; Hase, W. L. *Chemical Kinetics and Dynamics*; Prentice Hall: New York, 1989.
(108) Murdoch, J. R. *J. Chem. Educ.* **1981**, *58*, 32.
(109) Kozuch, S.; Shaik, S. *Acc. Chem. Res.* **2010**, *44*, 101.
(110) Comas-Vives, A.; Lledós, A.; Poli, R. *Chem.—Eur. J.* **2010**, *16*, 2147.
(111) Morse, P. M.; Spencer, M. D.; Wilson, S. R.; Girolami, G. S. *Organometallics* **1994**, *13*, 1646.
(112) Bell, G.; Janssen, A. E. M.; Halling, P. J. *Enzyme Microb. Technol.* **1997**, *20*, 471.
(113) French, H. T. *J. Chem. Thermodyn.* **1987**, *19*, 1155.
(114) Wakisaka, A.; Abdoul-Carime, H.; Yamamoto, Y.; Kiyozumi, Y. *J. Chem. Soc., Faraday Trans.* **1998**, *94*, 369.
(115) Oldiges, C.; Wittler, K.; Tönsing, T.; Alijah, A. *J. Phys. Chem. A* **2002**, *106*, 7147.
(116) Mountain, R. D. *J. Phys. Chem. B* **2010**, *114*, 16460.
(117) Stanbury, D. M.; Wilmarth, W. K.; Khalaf, S.; Po, H. N.; Byrd, J. E. *Inorg. Chem.* **1980**, *19*, 2715.
(118) Walker, J. A.; Zheng, L.; Knobler, C. B.; Soto, J.; Hawthorne, M. F. *Inorg. Chem.* **1987**, *26*, 1608.
(119) Schoenfeldt, N. J.; Ni, Z.; Korinda, A. W.; Meyer, R. J.; Notestein, J. M. *J. Am. Chem. Soc.* **2011**, *133*, 18684.
(120) Owens, G. S.; Durazo, A.; Abu-Omar, M. M. *Chem.—Eur. J.* **2002**, *8*, 3053.
(121) Altmann, P.; Cokoja, M.; Kühn, F. E. *Eur. J. Inorg. Chem.* **2012**, 3235.
(122) Deubel, D. V.; Frenking, G.; Gisdakis, P.; Herrmann, W. A.; Rösch, N.; Sundermeyer, J. *Acc. Chem. Res.* **2004**, *37*, 645.
(123) Gisdakis, P.; Yudanov, I. V.; Rösch, N. *Inorg. Chem.* **2001**, *40*, 3755.